BBLN-1 is essential for intermediate filament organization and apical membrane morphology

Graphical abstract

Highlights

- BBLN-1 regulates intestinal lumen morphology in *C. elegans*

- BBLN-1 loss causes bubble-shaped membrane invaginations into the cytoplasm

- Abnormal intermediate filament aggregation drives cytoplasmic invaginations

- bublin (BBLN) is the mammalian ortholog of BBLN-1
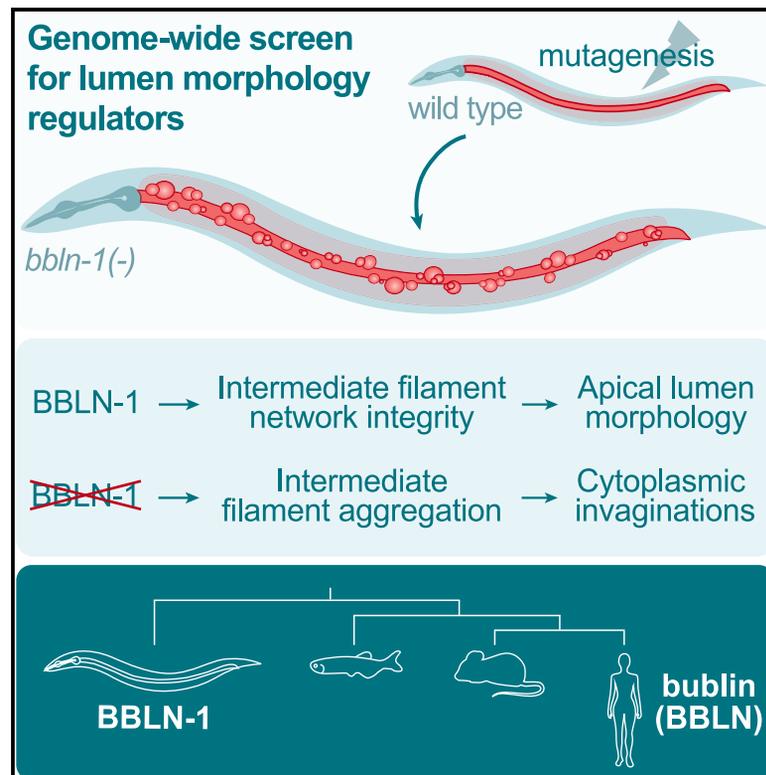
Authors

Sanne Remmelzwaal, Florian Geisler, Riccardo Stucchi, ..., Rudolf E. Leube, João J. Ramalho, Mike Boxem

Correspondence

joao.ramalho@wur.nl (J.J.R.), m.boxem@uu.nl (M.B.)

In brief

Remmelzwaal et al. identify BBLN-1, a novel regulator of intermediate filament organization in *C. elegans.* Loss of BBLN-1 leads to apical membrane invaginations into the cytoplasm of intestinal cells, likely caused by intermediate filament aggregation. They go on to show that bublin (BBLN) is the mammalian ortholog of BBLN-1.

CellPress

Article

BBLN-1 is essential for intermediate filament organization and apical membrane morphology

Sanne Remmelzwaal,[1] Florian Geisler,[2] Riccardo Stucchi,[3,4,8] Suzanne van der Horst,[5,6] Milena Pasolli,[3] Jason R. Kroll,[1] Olga D. Jarosinska,[1] Anna Akhmanova,[3] Christine A. Richardson,[7] Maarten Altelaar,[4] Rudolf E. Leube,[2] João J. Ramalho,[1,9,10,*] and Mike Boxem[1,10,11,12,*]

[1]Developmental Biology, Institute of Biodynamics and Biocomplexity, Department of Biology, Faculty of Science, Utrecht University, Padualaan 8, 3584 CH Utrecht, the Netherlands
[2]Institute of Molecular and Cellular Anatomy, RWTH Aachen University, 52074 Aachen, Germany
[3]Cell Biology, Neurobiology and Biophysics, Institute of Biodynamics and Biocomplexity, Department of Biology, Faculty of Science, Utrecht University, Padualaan 8, 3584 CH Utrecht, the Netherlands
[4]Biomolecular Mass Spectrometry and Proteomics, Bijvoet Center for Biomolecular Research and Utrecht Institute for Pharmaceutical Sciences, Utrecht University, Padualaan 8, 3584 CH Utrecht, the Netherlands
[5]Molecular Cancer Research, Center for Molecular Medicine, University Medical Center Utrecht, Utrecht University, Utrecht, the Netherlands
[6]Oncode Institute, Utrecht, the Netherlands
[7]Department of Biosciences, Durham University, Durham, UK
[8]Present address: Philochem AG, Libernstrasse 3, 8112 Otelfingen, Switzerland
[9]Present address: Laboratory of Biochemistry, Wageningen University & Research, Stippeneng 4, 6708 Wageningen, the Netherlands
[10]These authors contributed equally
[11]Twitter: @BoxemLab
[12]Lead contact
*Correspondence: joao.ramalho@wur.nl (J.J.R.), m.boxem@uu.nl (M.B.)
https://doi.org/10.1016/j.cub.2021.03.069

SUMMARY

Epithelial tubes are essential components of metazoan organ systems that control the flow of fluids and the exchange of materials between body compartments and the outside environment. The size and shape of the central lumen confer important characteristics to tubular organs and need to be carefully controlled. Here, we identify the small coiled-coil protein BBLN-1 as a regulator of lumen morphology in the *C. elegans* intestine. Loss of BBLN-1 causes the formation of bubble-shaped invaginations of the apical membrane into the cytoplasm of intestinal cells and abnormal aggregation of the subapical intermediate filament (IF) network. BBLN-1 interacts with IF proteins and localizes to the IF network in an IF-dependent manner. The appearance of invaginations is a result of the abnormal IF aggregation, indicating a direct role for the IF network in maintaining lumen homeostasis. Finally, we identify bublin (BBLN) as the mammalian ortholog of BBLN-1. When expressed in the *C. elegans* intestine, BBLN recapitulates the localization pattern of BBLN-1 and can compensate for the loss of BBLN-1 in early larvae. In mouse intestinal organoids, BBLN localizes subapically, together with the IF protein keratin 8. Our results therefore may have implications for understanding the role of IFs in regulating epithelial tube morphology in mammals.

INTRODUCTION

Epithelial and endothelial tubes are fundamental building units of many organs, including the digestive tract, vascular system, and lung. Tubular organs are essential for molecular transport and form protective barriers to the outside environment.[1–5] The *Caenorhabditis elegans* intestine provides a simple model to study the regulation of lumen morphology. It is composed of 20 cells arranged in nine segments surrounding a central lumen (Figure 1A).[6,7] Specialized cell-cell junctions connect neighboring cells and ensure impermeability of the lumen.[8] The intestinal cells are polarized along an apicobasal axis and resemble mammalian enterocytes at the ultrastructural level.[9] The lumen-forming apical surface of both cell types is covered by microvilli that contain bundled actin filaments and are supported by the subapical actin-rich terminal web.[7,10] The luminal surface is further supported by an intermediate-filament (IF) rich fibrous sheet that directly underlies—and is likely connected to—the terminal web.

The *C. elegans* IF network forms a particularly electron-dense structure anchored at the lateral cell junctions that is known as the "endotube."[9–11] Cytoplasmic IF proteins form resilient flexible networks that mediate mechanical properties of cells and tissues.[12,13] In tubular epithelia, subapical IF networks are ideally positioned to contribute to the regulation of lumen morphology and functioning.[13–17] In the *C. elegans* intestine, loss of IF subunits or of the IF organizers IFO-1 and SMA-5 can result in morphological abnormalities of the lumen and increased susceptibility to microbial, osmotic, and oxidative stresses.[18–21]
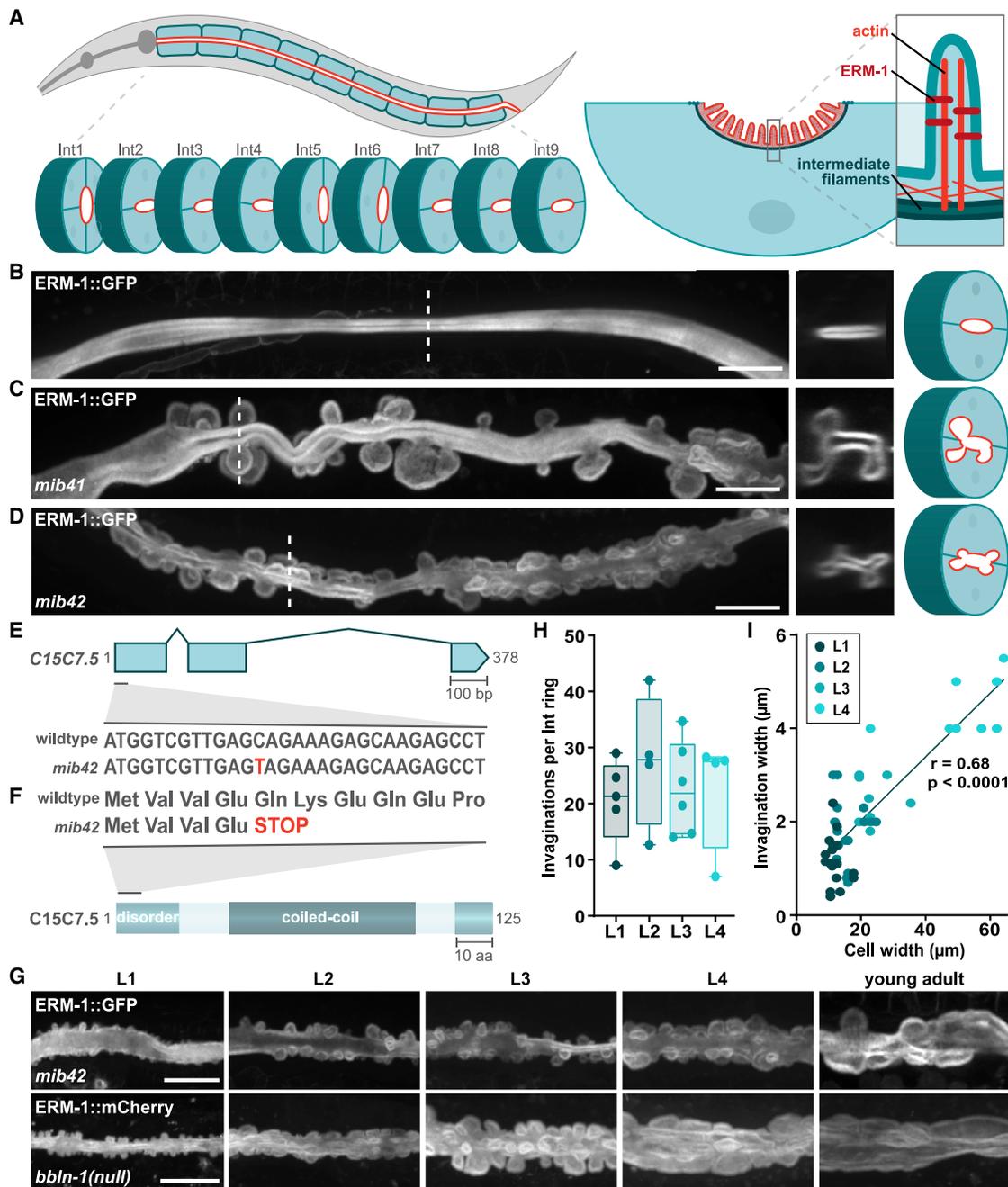
Figure 1. The intestines of *mib41* and *mib42* mutants show cytoplasmic invaginations

(A) Schematics of the *C. elegans* intestine and localization of proteins relevant for this study.

(B–D) Intestinal apical membrane morphology in L4 animals visualized by ERM-1::GFP. Dashed lines indicate position of cross-section. Schematics depict cross-section with apical membrane in red. Unless otherwise indicated, in this and all other figures, images were acquired using spinning-disk confocal microscopy, lateral views are maximum intensity projections, and anterior is to the left. All scale bars indicate 10 μm.

(E and F) Genomic structure of *C15C7.5* (E) and representation of the C15C7.5 protein with predicted domains (F).

(G) Progression of *mib42* and *bbln-1(null)* phenotypes visualized by ERM-1::GFP and ERM-1::mCherry, respectively.

(H) Quantification of invagination number in *bbln-1(null)* animals. Each point represents the average number of invaginations per intestinal ring in one animal. Data show median ± interquartile range. Differences are not significant (Kruskal-Wallis followed by Dunn's multiple comparisons test; p > 0.99).

(I) Correlation between cell and invagination width in *bbln-1(null)* animals, color coded per larval stage. Linear regression is shown for all data points combined. Data are analyzed with nonparametric Spearman correlation.

See also Figures S1 and S2 and Video S1.

Here, we report the identification of an evolutionary conserved regulator of intestinal tube morphology and IF organization we term *bbln-1*, for bulges budding from the intestinal lumen. *bbln-1* mutant intestines develop large invaginations of the apical lumen into the cytoplasm of intestinal cells. We show that these cytoplasmic invaginations are likely the result of an aggregated IF network state caused by loss of *bbln-1*. We also identified a mammalian ortholog of BBLN-1, which we termed bublin (BBLN). BBLN shares multiple candidate protein interaction partners with BBLN-1 and can partially substitute for BBLN-1 functioning in the *C. elegans* intestine. Our findings provide further evidence that the subapical IF network plays an active role in regulating the morphology of tubular epithelia, although the structural and functional conservation from *C. elegans* to humans provides a model for studying IF modulation *in vivo*.

RESULTS

Loss of *bbln-1* causes cytoplasmic invaginations of the intestinal apical membrane

In a genetic screen for lumen morphology defects, we identified two viable mutants (*mib41* and *mib42*) with dramatic bubble-shaped protrusions of the apical plasma membrane into the cytoplasm of *C. elegans* intestinal cells (Figures 1A–1D). Complementation analysis indicated that *mib41* and *mib42* affect different loci. Through single-nucleotide polymorphism mapping and whole-genome sequencing,[22,23] we identified a single cluster of candidate mutations for each allele.

For *mib41*, only one candidate mutation was predicted to exert a detrimental effect on protein function: an arginine to tryptophan substitution in the kinase domain of SMA-5 (Arg124Trp in SMA-5a; Figure S1A). *sma-5* mutations induce a lumen invagination phenotype similar to *mib41* mutants,[21] and the *sma-5(n678)* allele[24] failed to complement *mib41*. Thus, *mib41* is a novel *sma-5* allele.

The *mib42* sequencing data also yielded a single potentially deleterious mutation within a predicted open reading frame (ORF): an early stop at the fifth codon of the uncharacterized gene *C15C7.5* (Figures 1E and 1F). *C15C7.5* RNA interference (RNAi) phenocopied *mib42* (Figure S1B), and transgenic expression of *GFP::C15C7.5* from the intestine-specific *vha-6* promoter rescued the invagination phenotype of *mib42* (Figure S1C). We used CRISPR-Cas9 to generate the *mib70*-null allele that removes the C15C7.5 coding sequence, from here on referred to as *C15C7.5(null)*. The *C15C7.5(null)* allele caused cytoplasmic invaginations (Figure S1D) and did not complement *mib42*. Together, these data show that *mib42* is an allele of *C15C7.5*. The invagination phenotype in *C15C7.5(null)* animals was more severe than in *mib42* mutants (Figure 1G), indicating that *mib42* is a partial loss-of-function mutation. We named the *C15C7.5* gene *bbln-1* for bulges budding from the intestinal lumen.

bbln-1(null) animals are homozygous viable but somewhat developmentally delayed (Figures S1E and S1F). This delay is likely a consequence of the intestinal abnormalities, as intestinal expression of GFP::BBLN-1 nearly fully rescued the developmental delay (Figures S1E and S1F). In *bbln-1(null)* animals, invaginations were visible from hatching, and the number of invaginations remained constant throughout development (Figures 1G

and 1H). Time-lapse imaging showed that the invaginations were stable over a period of several hours (Video S1). Invagination width correlated with intestinal cell width, and in late larval and adult stages, invaginations had an elongated appearance (Figure 1I). The *bbln-1* invaginations were spread uniformly along the length of the intestine (Figures 1D and 1G). However, in cross-section, invaginations seemed to preferentially localize at the vertices of the ellipse-shaped lumen, in proximity to cell junctions. This was particularly noticeable in *mib42* animals, which have fewer invaginations than *bbln-1(null)* mutants (Figure 1D). Visualizing invaginations in a *bbln-1(mib42)* strain expressing the junctional marker DLG-1::mCherry confirmed that invaginations occurred in proximity to cell junctions (Figures S2A–S2D).

To assess intestine morphology and integrity, we fed animals with three sizes of Texas Red-dextran conjugates (3 kDa, 10 kDa, and 40 kDa). In wild-type animals, Texas Red signals filled the lumen (Figures S2E–S2G). In *bbln-1(mib42)* animals, all invaginations contained Texas Red signal, indicating that they are contiguous with the lumen. We never observed internalized invaginations or presence of Texas Red signal in the cytoplasm of intestinal cells, indicating that the invaginations are not internalized. We also did not observe paracellular passage of conjugates in the intestine (Figures S2F and S2G). This contrasted with the pharynx, where we observed paracellular passage of the 3-kDa conjugate in both wild-type and *bbln-1* animals (Figures S2H and S2I). These data indicate that paracellular permeability of the intestine is not significantly affected by loss of BBLN-1.

BBLN-1 is a small coiled-coil protein that localizes dynamically to IF-rich structures

bbln-1 is predicted to encode a single protein isoform of just 125 amino acids (aas) with a central coiled-coil domain (aas 39–102) flanked by intrinsically disordered regions (Figure 1F). To investigate the localization pattern of BBLN-1, we engineered an endogenous BBLN-1::GFP fusion. Homozygous *gfp::bbln-1* animals show no intestinal lumen defects or developmental delay (Figures S1E and S1F), demonstrating that GFP::BBLN-1 is functional. In contrast, a C-terminally tagged BBLN-1::mKate2 variant proved non-functional.

BBLN-1 was first apparent at the comma stage of embryonic development, at the apical domain of intestinal cells (Figure 2A). In subsequent embryonic stages, BBLN-1 became visible in the hypodermis and pharynx as well. In larval and adult stages, we detected BBLN-1 in many epithelial tissues, including the pharynx, intestine, excretory canal, and hypodermis (Figure 2B). In each of these tissues, the distribution of BBLN-1 was similar to previously reported distributions of IF proteins.[8,25–28] To investigate the localization of BBLN-1 relative to IFs, we engineered an endogenous IFB-1::mCherry fusion. Close overlap between GFP::BBLN-1 and IFB-1::mCherry in each tissue indicates that BBLN-1 indeed localizes to IFs (Figures S3A–S3C).

In the intestine, BBLN-1 localized subapically and at cell junctions (Figure 2Biv), suggesting localization to the endotube.[10] We therefore generated an endogenous IFB-2::mCherry fusion and analyzed the localization of BBLN-1 relative to IFB-2 and ERM-1, which localizes to microvilli.[29,30] Consistent with localization to the endotube, we found that BBLN-1 co-localized with IFB-2, basal to ERM-1 (Figures 2C and 2D). To determine whether
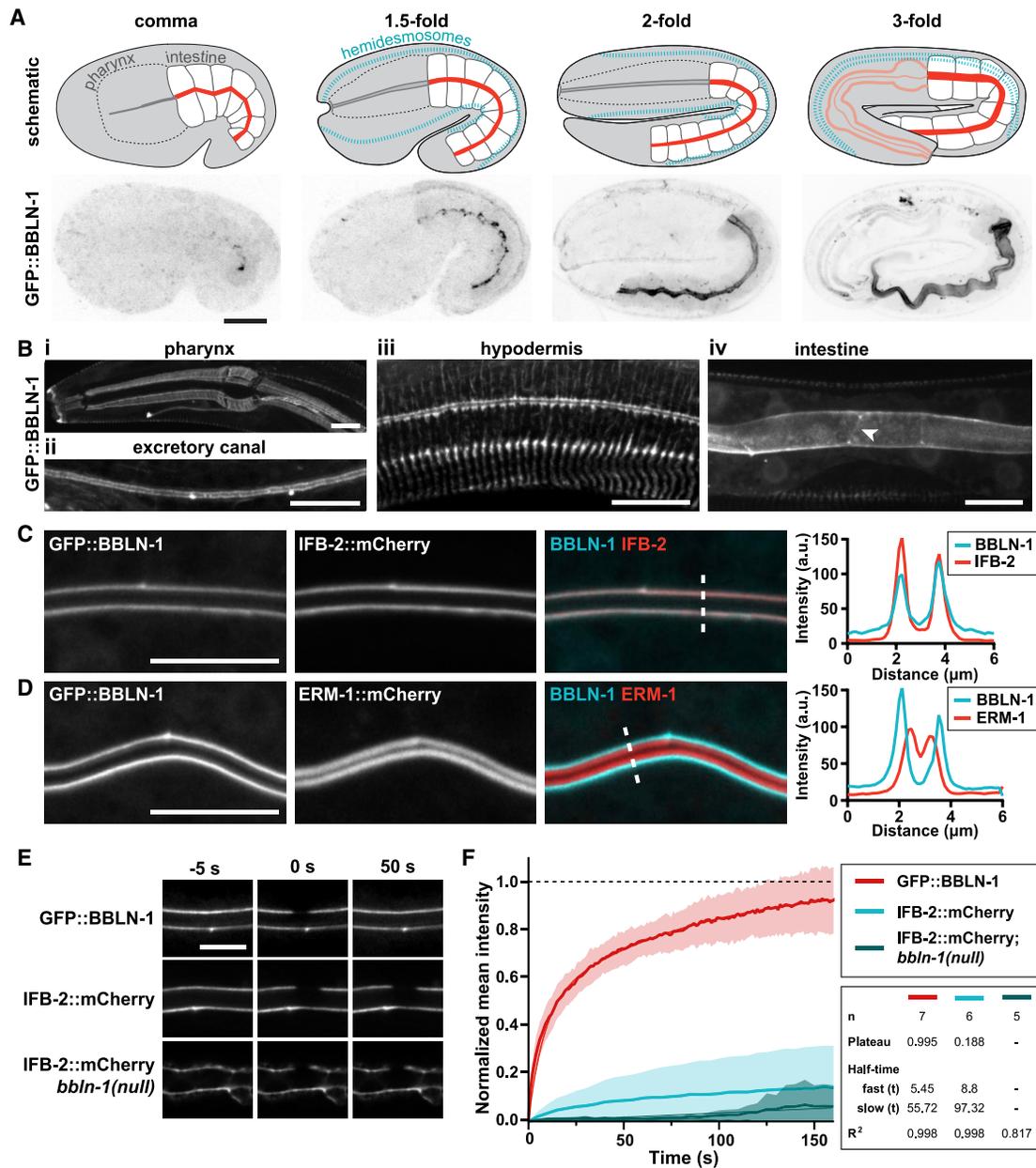
Figure 2. BBLN-1 localizes dynamically to IF-rich structures

(A and B) Distribution of GFP::BBLN-1 during late embryonic development (A) and in different tissues in late L3–young adult animals (B). Arrowhead indicates apical junction. All scale bars indicate 10 μm.

(C and D) Distribution of GFP::BBLN-1 compared with ERM-1::mCherry (C) and IFB-2::mCherry (D) at the apical domain of intestinal cells of L3 larvae. Dashed lines indicate sites of intensity profiles.

(E and F) Stills from time-lapse imaging (E) and FRAP curves (F). Time-lapse data were acquired at 1-s intervals for GFP::BBLN-1 and 5-s intervals for IFB-2::mCherry. Thin lines and shading represent the mean ± SD. No plateau or half-times could be accurately determined for IFB-2::mCherry; *bbln-1(null)*.

See also Figure S3.

BBLN-1 stably associates with the IF network, we performed fluorescence recovery after photobleaching (FRAP) experiments. IFB-2 recovered only ∼15% in 150 s (Figures 2E and 2F). Similar slow recovery was reported for IFA-1 and IFB-1 in the pharynx.[27] In contrast, BBLN-1 recovered ∼90% within the same period. Together, these results indicate that BBLN-1 is a dynamic component of the endotube in intestinal cells.

The subcellular localization of BBLN-1 depends on IFs

We next determined whether the apical localization of BBLN-1 depends on IFs. We used RNAi feeding to knock down each of the six intestinal IF proteins that are part of the endotube.[10,19,31,32] We observed significant reduction in apical BBLN-1 upon knockdown of IFB-2, IFD-1, IFD-2, or IFP-1 (Figures 3A and 3B). In *ifb-2(RNAi)* animals, the loss of BBLN-1
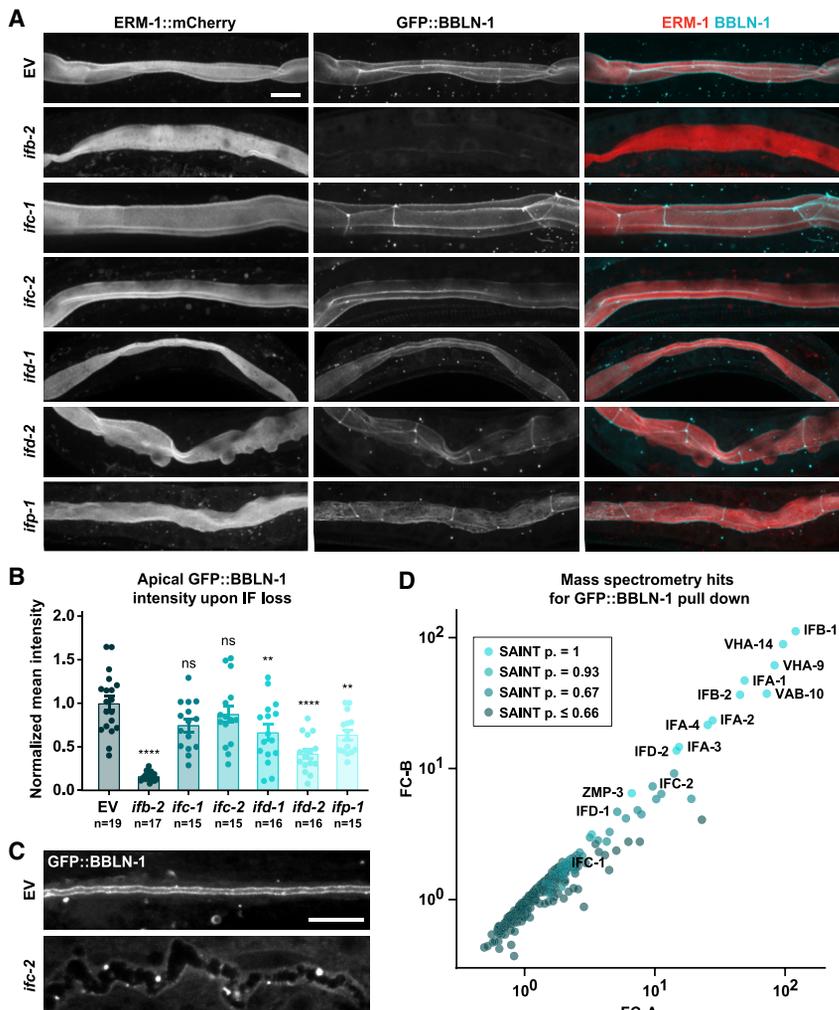
Figure 3. BBLN-1 requires IFs for its apical localization in the intestine

(A) Intestinal GFP::BBLN-1 distribution and apical membrane morphology, visualized by ERM-1::mCherry, upon RNAi knockdown of targets indicated to the left. EV, empty vector. All scale bars indicate 10 μm.

(B) Quantification of GFP::BBLN-1 levels at the intestinal apical domain of larvae subjected to RNAi. Each data point represents the average of six or eight measurements in a single animal. Data are presented as mean ± SEM and analyzed with ordinary one-way ANOVA followed by Dunnett's multiple comparisons test; ns, $p > 0.05$; **$p < 0.005$; ****$p < 0.0001$.

(C) GFP::BBLN-1 distribution in the excretory canal upon RNAi knockdown of *ifc-2* or EV control.

(D) Mass spectrometry hits for GFP::BBLN-1 pull-down plotted as correlation between fold-change (FC) score A and more stringent FC score B. Data points are color coded for different SAINT probability scores.

See also Figure S6.

C. elegans intestine.[10,18,33,34] We depleted each protein by RNAi in strains expressing ERM-1::mCherry or IFB-2::mCherry, together with GFP::BBLN-1. In each case, the localization of BBLN-1 mimicked the localization pattern of IFB-2, including basolateral mislocalization in *let-413(RNAi)* embryos (Figures 4A–4C). This confirms that BBLN-1 associates with IFs.

In *sma-5(RNAi)* intestines, we observed a significant reduction of cortical BBLN-1 levels (Figure 4D). This suggests that *sma-5* acts upstream of *bbln-1*. However, inactivation of *sma-5* by RNAi in a *bbln-1(null)* background resulted in more severe intestinal abnormalities than either *sma-5(RNAi)* or *bbln-1(null)* alone (Figure 4E). Thus, although *sma-5* may act in part through *bbln-1*, these genes also have independent functions.

Collectively, the dependence on IFs, the co-localization of BBLN-1 with aberrantly localized IFB-2, and the co-purification of BBLN-1 with IF proteins suggest that BBLN-1 associates with the IF network.

Loss of *bbln-1* compromises the integrity of the IF network

To investigate whether apical domain invaginations in *bbln-1* mutants were associated with defects in intestinal IF organization, we analyzed the distribution of IFB-2, IFC-2, and IFD-2 in *bbln-1(null)* animals. In control animals, IFB-2 and IFC-2 were distributed evenly along the adluminal domain and were enriched at cell junctions (Figures 5A and 5C). These localization patterns match prior observations.[18,19,21,35] In contrast, IFD-2 showed a punctate localization pattern and was excluded from cell junctions (Figures 5E and S5A), indicating functional specialization within the IF network. Upon loss of *bbln-1*, all three IF proteins retained their subapical localization but formed a network

was most striking. IFB-2 is an essential component of the apical intestinal IF network, and loss of IFB-2 results in a complete absence of the endotube.[19,20] Therefore, the strong reduction in apical BBLN-1 likely reflects the loss of all IFs from the apical domain. We also examined BBLN-1 in the excretory canal of *ifc-2(RNAi)* animals, as IFC-2 has been shown to be important for the structure of this tissue.[25] We observed relocalization of BBLN-1 from the apical cortex to the cytoplasm and basal membrane, which suggests that dependency on IFs is a general aspect of BBLN-1 localization (Figure 3C).

The reliance of BBLN-1 localization on an intact IF network indicates a potential association with IF proteins. To identify candidate interacting proteins, we performed affinity purification of GFP::BBLN-1 from mixed-stage *C. elegans* cultures, followed by mass spectrometry analysis. Consistent with the localization and dependency on IFs, the highest ranking proteins identified included all intestinal IF proteins except IFP-1 (Figure 3D).

To further confirm the dependency of BBLN-1 on IFs, we examined the effects of inactivation of known regulators of IF organization on BBLN-1. In addition to *sma-5*, loss of *ifo-1*, *act-5*, and *let-413* have all been reported to disrupt IFB-2 distribution in the
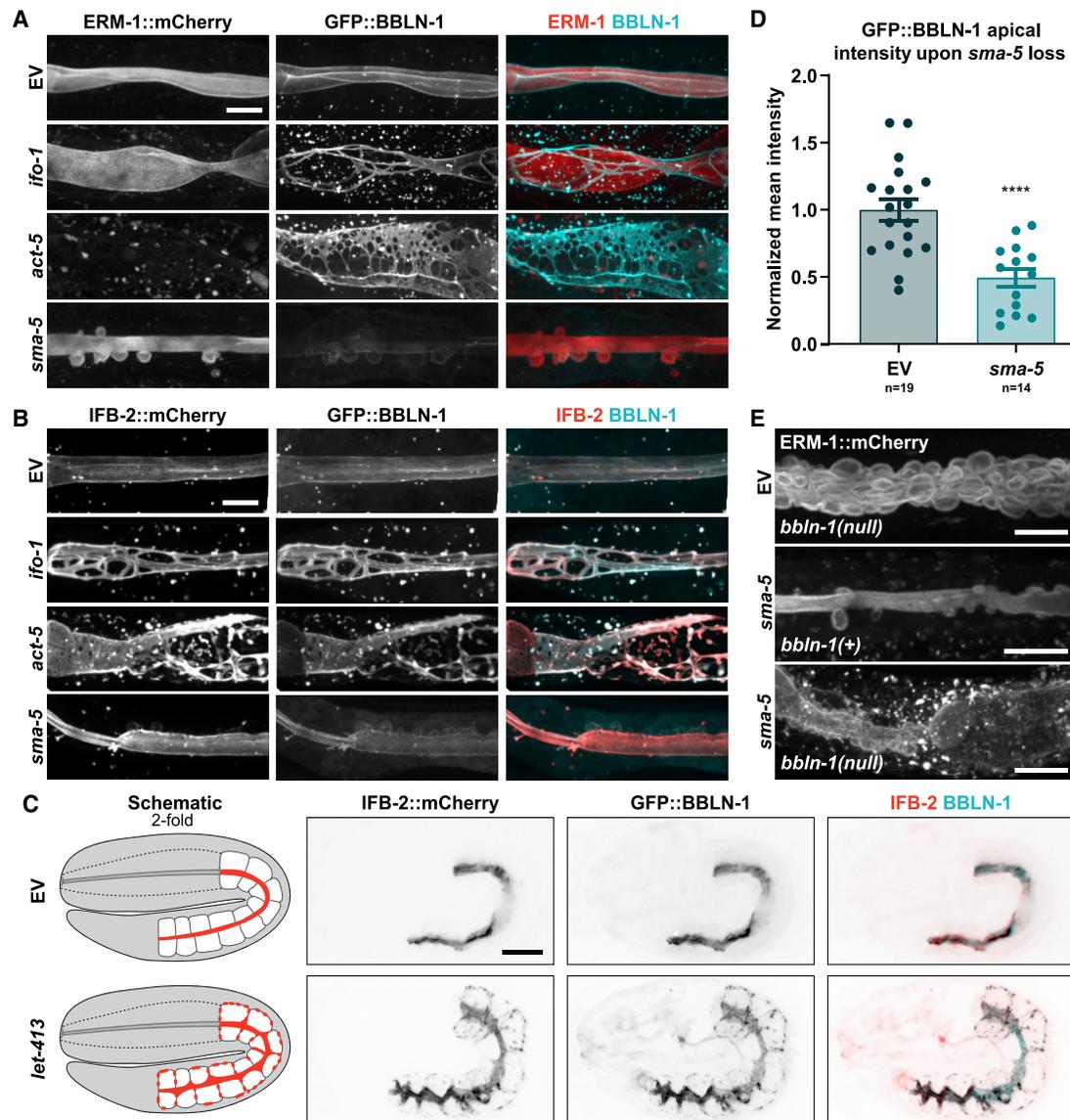
Figure 4. BBLN-1 co-localizes with mislocalized IFs

(A) Intestinal GFP::BBLN-1 distribution and apical membrane morphology, visualized by ERM-1::mCherry, after RNAi knockdown of targets indicated on the left. Same control is shown as in Figure 3A because data are from a single experiment. All scale bars indicate 10 μm.

(B and C) GFP::BBLN-1 and IFB-2::mCherry distribution in L2–L4 larvae (B) and 2-fold embryos (C) after RNAi knockdown of targets indicated on the left.

(D) Quantification of GFP::BBLN-1 levels at the intestinal apical domain of L3/L4 larvae subjected to RNAi knockdown of *sma-5*. Each data point represents the average of six or eight measurements in a single animal. Data show mean ± SEM. Ordinary one-way ANOVA followed by Dunnett's multiple comparisons test, ****$p < 0.0001$. EV control data are same as in Figure 3B.

(E) Apical membrane morphology, visualized by ERM-1::mCherry, after RNAi knockdown of targets indicated on the left in *bbln-1(+)* or *bbln-1(null)* background.

of cables or bundles surrounding protrusions into the cytoplasm (Figures 5B, 5D, and 5F). To investigate the stability of IFs within the aggregated bundles, we performed FRAP on IFB-2::mCherry in *bbln-1(null)* animals. IFB-2 showed very little fluorescence recovery, appearing, if anything, even more stable than in control animals (Figures 2E and 2F). Together, these data indicate that BBLN-1 is required for the integrity of the IF network, but not for IF recruitment to the subapical cortex.

Loss of BBLN-1 did not cause defects in the organization of the IF network in the pharynx or hypodermis (Figures S4A–

S4C). The only minor effect we noticed was in the excretory canal, where IFB-1::mCherry puncta of unknown nature were absent in *bbln-1* mutants (Figure S4D). The lack of severe defects in other tissues indicates that the intestinal IF network is uniquely sensitive to BBLN-1 loss.

To investigate whether BBLN-1 is required for IF network integrity throughout development, we used the auxin-inducible degradation (AID) system.[36,37] We tagged BBLN-1 with GFP and the AID-degron and expressed TIR1 from the intestine-specific *elt-2* promoter. Within 1 h of auxin addition to L1-stage
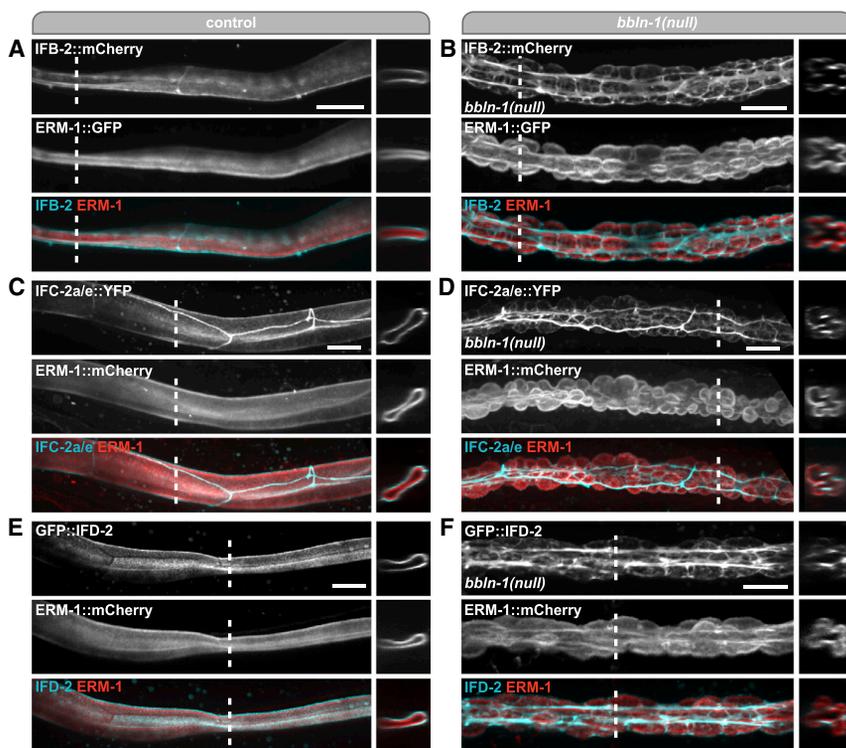
Figure 5. Loss of *bbln-1* compromises the integrity of the IF network

Organization of the intestinal IF network visualized with IFB-2::mCherry (A and B), IFC-2a/e::YFP (C and D), or GFP::IFD-2 (E and F) in control (A, C, and E) or *bbln-1(null)* (B, D, and F) animals. Large panels are lateral views, and small panels are cross-sections at the site indicated by the dashed lines. All scale bars indicate 10 μm. See also Figures S4 and S5.

To confirm loss of IF network integrity in *bbln-1* mutants, we performed electron microscopy (EM). As previously reported for *sma-5* mutant intestines, the endotube in *bbln-1(null)* animals was lost or diminished at sites of invagination and thickened around the base of invaginations (Figure 6, compare A versus B or C versus D).[21] Nevertheless, as in wild-type animals, aggregated endotube material in *bbln-1(null)* intestines still maintained a distance from the apical membrane, consistent with the continued presence of the subapical terminal web (Figures 6A and 6B, inlays). Finally, similar to *ifb-2* mutants,[20] microvilli were still abundant in invaginations, showing that *bbln-1* and a fully assembled endotube are not required for microvilli formation.

Taken together, the EM and light microscopy observations demonstrate that the intestinal IF network collapses and aggregates into stable bundles upon loss of BBLN-1, without affecting other aspects of intestinal epithelial polarity or the actin cytoskeleton.

animals, apical GFP::AID::BBLN-1 was no longer detectable (Figure S5B). We next added auxin to late L1 stage or early L4 stage animals and imaged the intestinal lumen after 24 and 48 h (Figure S5C). Irrespective of the starting time point, approximately half of the animals had developed invaginations after 24 h of auxin treatment (Figure S5D; 48-h time point). The remainder showed small "holes" in the IFB-2::mCherry fluorescent pattern (Figure S5E). Eventually, all animals treated with auxin from L1 developed cytoplasmic invaginations (Figure S5D; 72-h time point). These data show that *bbln-1* is required to maintain the integrity of the IF network throughout development.

We also investigated whether re-expression of BBLN-1 could revert already formed invaginations. We hatched GFP::AID::BBLN-1 animals in the presence of auxin and transferred L1 animals to plates lacking auxin. BBLN-1 levels recovered within 24 h (Figure S5F). However, we still observed invaginations in L4 and adult animals (Figures S5G and S5H). Presence of BBLN-1 is therefore not sufficient to restore an already malformed luminal domain.

To investigate whether *bbln-1* loss affects apical actin distribution or cell polarity, we examined the localization of the intestinal actin ACT-5 and the polarity proteins LET-413/Scrib and PAR-6. In *bbln-1(null)* animals, ACT-5 smoothly decorated the surface of the cytoplasmic invaginations and was not enriched in bundles or cables (Figures S5I and S5J). Inactivation of *bbln-1* by RNAi also did not affect the basolateral localization of LET-413 or the apical localization of PAR-6 (Figures S5K and S5L). Thus, loss of BBLN-1 does not disrupt the terminal web or microvillar actin, and the effects of *bbln-1* on the IF network are not due to a loss of intestinal polarity.

Apical IF aggregation drives cytoplasmic invaginations

We next sought to better understand the relationship between the cytoplasmic invaginations and collapsed IF network. If invaginations are a consequence of the IF network collapse, direct disruption of the IF network might similarly cause invaginations. As recently reported,[19] *ifd-2(RNAi)* induced cytoplasmic invaginations, though with much lower penetrance and severity than *bbln-1* mutants (Figure 3A). To determine whether invaginations in *ifd-2(RNAi)* animals are due to the partial loss of BBLN-1, we performed *ifd-2(RNAi)* in a *bbln-1(null)* mutant background. The combined loss of *ifd-2* and *bbln-1* resulted in more severe lumen abnormalities than loss of *bbln-1* alone (Figure S6A), indicating that both genes have at least partially independent functions. These data support the hypothesis that cytoplasmic invaginations in *bbln-1* mutants are caused by defects in the IF network.

Surprisingly, despite the loss of the complete intestinal IF network, *ifb-2* knockout animals display only mild intestinal lumen morphology defects.[19] We similarly observed an irregular lumen morphology in only a subset of *ifb-2(RNAi)* animals and no cytoplasmic invaginations (Figures 3A and S6B). If the *bbln-1* invaginations are due to an altered IF network state, loss of the IF
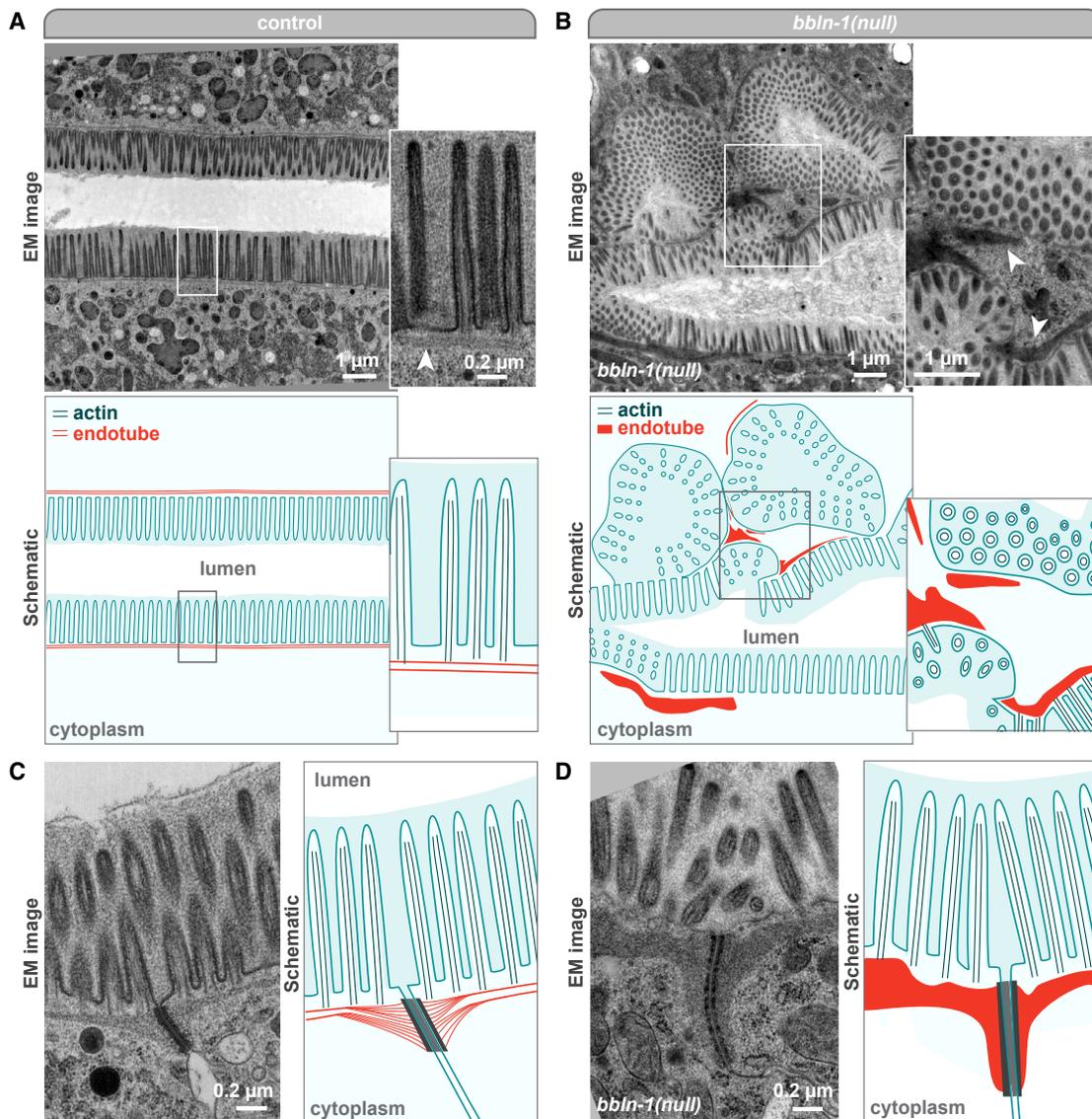
Figure 6. Loss of *bbln-1* compromises the integrity of the endotube

Ultrastructure of the apical domain (A and B) and apical junctions (C and D) in intestinal cells of *bbln-1(+)* and *bbln-1(null)* adult animals visualized by transmission electron microscopy. Boxed region is shown enlarged, and arrowheads point to the endotube. Schematics indicate actin bundles in dark blue, endotube in red, and junction in gray.

network should suppress the *bbln-1* phenotype. Indeed, lumen morphology in an *ifb-2(kc14); bbln-1(null)* double mutant appeared identical to that seen upon loss of IFB-2 (Figures 3A and S6C).[19] We also did not observe cytoplasmic invaginations in the double mutant by EM (Figure S6D). No endotube was visible, confirming the requirement for IFB-2 in endotube formation. We did observe occasional small-membrane protrusions directed toward the lumen (Figure S6E), which were also visible by light microscopy in both *ifb-2(kc14); bbln-1(null)* (Figure S6F) and *ifb-2(RNAi)* animals (Figure S6Biii). These are therefore likely to be the result of IFB-2 depletion alone.

Together, our data are consistent with a model in which loss of *bbln-1* leads to an altered, pathogenic IF network state that results in cytoplasmic invaginations.

BBLN is the mammalian ortholog of BBLN-1

To investigate whether BBLN-1 is conserved in mammals, we performed an iterative homology search using Jackhmmer.[38] The uncharacterized protein C9orf16 was the only candidate mammalian homolog (E-value 3.8e−16). The 83-aa human C9orf16 protein is predicted to consist of a coiled-coil domain, flanked by intrinsically disordered regions—similar to BBLN-1 (Figure 7A). A reciprocal Jackhmmer search identified BBLN-1 as the only *C. elegans* homolog of C9orf16 (E-value 8.4e−07). Given the bi-directional best hit and absence of other candidate orthologs, we consider it likely that BBLN-1 and C9orf16 are evolutionary orthologs and we have named the human gene product bublin coiled-coil protein (BBLN).
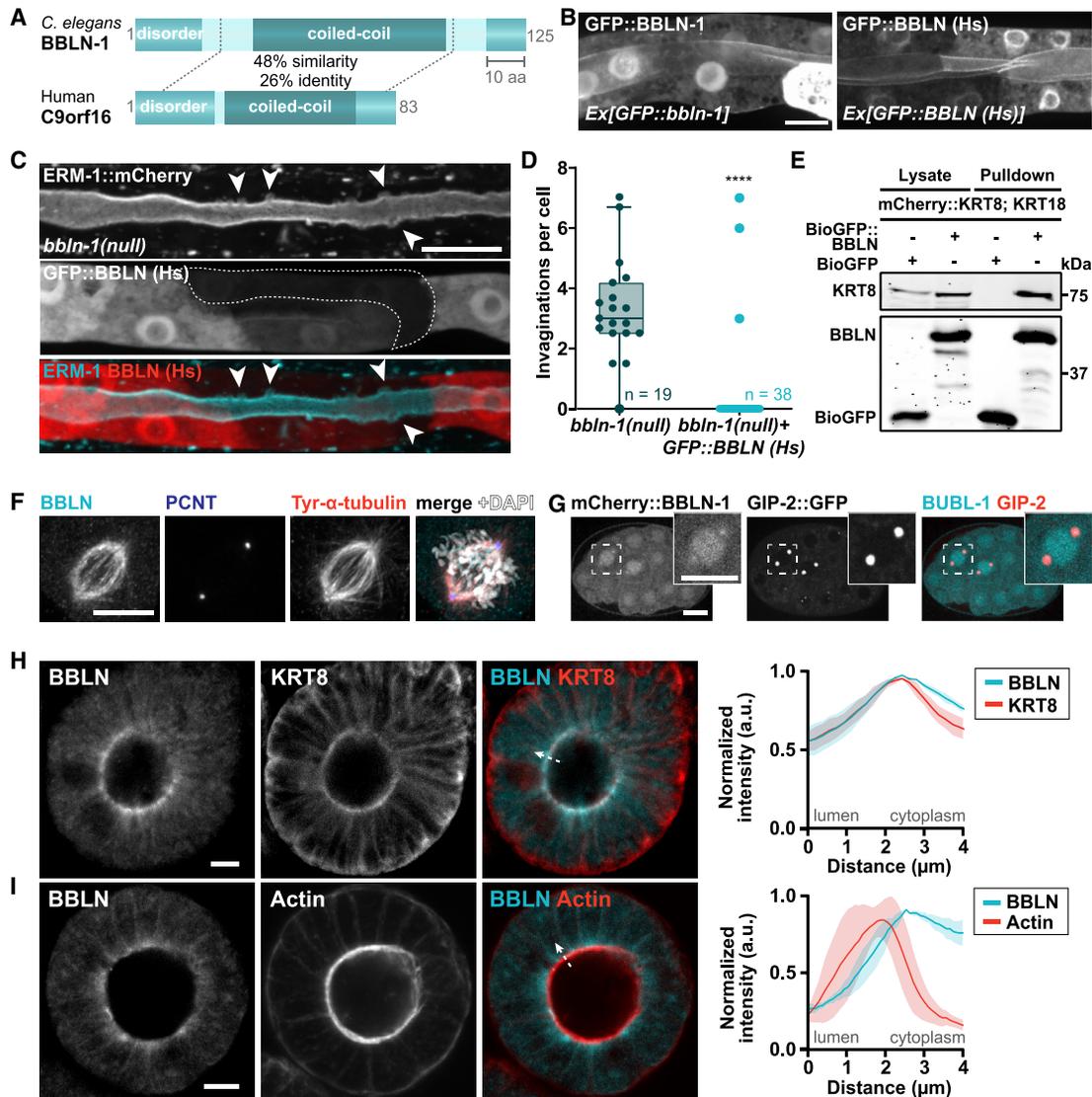
Figure 7. Bublin is the mammalian homolog of BBLN-1

(A) Schematic of *C. elegans* BBLN-1 and human C9orf16 proteins.

(B) Overexpression of GFP-tagged BBLN-1 and bublin (BBLN [Hs]) in *C. elegans* L3-stage larvae driven by the intestine-specific *vha-6* promoter. All scale bars indicate 10 μm.

(C) Apical membrane morphology visualized by ERM-1::mCherry in a *bbln-1(null)* L1 larva with mosaic expression of GFP-tagged BBLN (Hs) from an extra-chromosomal array. A cell without GFP::BBLN (Hs) expression (dotted outline) displays cytoplasmic invaginations (arrowheads).

(D) Quantification of invagination number in *bbln-1(null)* early L1 intestinal cells with or without GFP::BBLN (Hs) expression. Analysis was performed within 4 h of hatching. Each dot corresponds to a single cell. Data show median ± interquartile range with Tukey whiskers. Mann-Whitney test, ****p < 0.0001.

(E) Western blots of Biotin pull-down from extracts of HEK293T cells transfected with BirA, mCherry::KRT8, KRT18, and either BioGFP::BBLN or BioGFP alone as control. Blots were probed for KRT8 (top) and GFP (bottom). Input is 10% of the biotin pull-down.

(F) Point-scanning confocal microscopy images of HeLa cell stained for BBLN, pericentrin (PCNT), and tyrosinated α-tubulin.

(G) mCherry::BBLN-1 and GIP-2::GFP distribution in the early *C. elegans* embryo.

(H and I) Section of mouse small intestinal organoid immunostained for BBLN and KRT8 (top) or with phalloidin to visualize actin (bottom). Images were acquired using point-scanning confocal microscopy. Graphs show fluorescent intensity from lumen to cytoplasm (dotted arrow indicates example). Fluorescent intensity was measured across all cells that are in focus and displayed as mean ± SD.

See also Figure S7.

To investigate whether BBLN and BBLN-1 are functionally conserved, we expressed GFP::BBLN in the intestine of *C. elegans* from an extrachromosomal array. BBLN showed apical and perinuclear enrichment, as did GFP::BBLN-1 when expressed from an extrachromosomal array (Figure 7B). Moreover, the subapical localization of BBLN was dependent on the presence of an IF network (Figure S7A). To determine whether BBLN can functionally replace BBLN-1, we expressed

GFP::BBLN in a *bbln-1(null)* background. *bbln-1(null)* animals all show invaginations from hatching (Figure 7D). In contrast, cells expressing GFP::BBLN did not show invaginations at hatching (Figures 7C and 7D). As animals developed, invaginations formed in all cells, and animals became phenotypically indistinguishable from non-transgenic animals by mid-L1 stage. Thus, expression of BBLN delays the invagination phenotype in young larvae. Together, these findings indicate that BBLN is a functional homolog of BBLN-1.

We next investigated whether the association with IFs is conserved. Keratin 8 (KRT8) is the most common type II keratin IF in simple epithelia, and in enterocytes, KRT8 is part of an apical IF network.[39] As KRT8 forms functional heterodimers with KRT18,[40] we investigated whether BBLN interacts with KRT8/18 by affinity purification. Pull-down analysis from HEK293T cell lysates showed that KRT8/18 co-purify with BBLN (Figure 7E). Additionally, multiple high-throughput studies found BBLN as an interactor of the type I intestinal KRT20.[41–43] Thus, the association with IFs is conserved between BBLN-1 and BBLN.

We also performed mass spectrometry analysis on BBLN purified from HEK293T cells. The top scoring hit was V-ATPase subunit D (ATP6V1D), the ortholog of *C. elegans* VHA-14 and second highest scoring hit in our BBLN-1 interaction screen (Figures S7B and 4D). We additionally found subunit F of this complex (ATP6V1F), the ortholog of the high-confidence BBLN-1 interactor VHA-9. Thus, BBLN-1 and BBLN share overlapping candidate interaction partners.

Finally, we investigated the subcellular localization of BBLN in mammalian cells using a GFP::BBLN expression construct and a polyclonal antibody directed against human BBLN. In HeLa cells expressing GFP::BBLN, immunostaining and GFP fluorescence patterns overlapped, demonstrating that the antibody recognizes BBLN (Figure S7C). We next immunostained HeLa cells for BBLN and KRT8. However, we did not detect overlap between the BBLN and KRT8 localization patterns (Figure S7D). Thus, whereas *C. elegans* BBLN-1 appears to exclusively co-localize with IFs, this is not the case for BBLN. Interestingly, in dividing HeLa cells, BBLN localized to interpolar and kinetochore microtubules, a localization we had not observed for BBLN-1 (Figure 7F). We re-examined the localization of BBLN-1 in *C. elegans* embryonic mitotic cells also expressing the centrosome marker GIP-2::GFP/γ-tubulin. BBLN-1 was enriched at the interpolar region (Figure 7G), indicating that both BBLN-1 and BBLN operate at the mitotic spindle.

HeLa cells do not contain the subapical IF web present in *C. elegans* intestinal cells and in differentiated enterocytes. We therefore examined the localization of BBLN in mouse small intestinal organoids, which mimic the normal structure and composition of the intestinal epithelium more closely. In organoids, BBLN showed clear enrichment at the apical domain of intestinal epithelial cells. BBLN localized just below the apical actin network, at the same level as KRT8 (Figures 7H and 7I). Thus, the localization of BBLN in mouse intestinal organoids mimics that of BBLN-1 in *C. elegans* intestinal cells. Collectively, the overlap in localization, rescue of phenotype, and similarity in putative interaction partners suggest that BBLN and BBLN-1 have at least partially overlapping functionality.

DISCUSSION

Using an unbiased approach in the animal model *C. elegans*, we identified the small protein BBLN-1 as a regulator of IFs and tubular architecture of the intestinal epithelium. Loss of *bbln-1* causes a disorganized IF network organization. Strikingly, loss of the apical IF network through knockout of *ifb-2* suppressed the *bbln-1* phenotype, demonstrating that the presence of apical IFs is a prerequisite for invagination formation. The most likely explanation is that *bbln-1* causes an altered, pathogenic IF network state that leads to the formation of invaginations into the cytoplasm. When we were preparing this work for publication, it came to our attention that some similar observations were made in a dissertation that describes the identification of a mutant carrying the same point mutation present in *bbln-1(mib42)*.[44]

We also identified C9orf16 as the mammalian ortholog of BBLN-1 and named it bublin coiled-coil protein (BBLN). Expression of BBLN was able to partially suppress the *bbln-1* phenotype, indicating functional conservation. Although BBLN-1 seems to strictly co-localize with IFs in *C. elegans*, this is not the case for BBLN. BBLN localized at the level of IFs in mouse intestinal organoids, but we did not observe co-localization with KRT8 in HeLa cells. Thus, although BBLN may regulate IF organization, its functioning may have diverged between *C. elegans* and mammals.

Why a compromised IF network leads to cytoplasmic invaginations is not clear. One explanation is that pressure from the lumen physically forces invaginations through weak spots in the IF network. However, *ifb-2* mutants that lack an apical IF network entirely have a largely normal intestinal morphology and do not show lumen widening until the L4 stage.[19] Possibly, the actin network compensates for the loss of the IF network and delimits luminal widening. The presence of compensatory mechanisms involving actin is supported by the observation that loss of *ifb-2* leads to an increase in apical levels of the actin-bundling protein plastin 1 (PLST-1).[19] Another explanation for the formation of invaginations is that the IF network plays a more-direct instructive role in determining the width of the lumen or the surface area of the apical membrane. Such a role has recently been proposed for the excretory canal, where IFs work in conjunction with actin and tubulin to control intracellular lumenogenesis.[26] Here, IFs are hypothesized to regulate access of membrane formation promoting vesicles to the lumen to restrain lateral lumen expansion. Defects in apical membrane trafficking in the intestine have been shown to cause ectopic lateral lumen formation.[45] Hence, it is possible that the IF network plays a role in apical trafficking in the intestine.

The molecular nature of the change to the IF network in *bbln-1* mutants also remains to be determined. The protein sequence of BBLN-1 does not clearly hint at its function, but possible roles include cross-linking or stabilizing IF filaments and anchoring of IFs to components of the overlying terminal web. The tendency of invaginations to occur at cell junctions may also indicate a role in linking IFs to cell junctions. However, our FRAP data indicate that BBLN-1 associates dynamically with the IF layer. Hence, the activities of BBLN-1 may be more indirect, for example, localizing unidentified regulators to the IF network or promoting post-translational modifications of IFs. Our

interaction studies identified subunits of V-ATPases as prominent candidate interactors of BBLN-1 and BBLN. Whether these interactions are indeed involved in IF regulation or other aspects of BBLN-1/BBLN function remains to be determined. A final intriguing hypothesis is that BBLN-1 is involved in protein aggregation. BBLN was found in a search for highly heat-resistant proteins that protect different subsets of proteins from aggregation or denaturation under stress conditions.[46] Indeed, BBLN is differentially expressed in diseases characterized by protein aggregation, including amyotrophic lateral sclerosis (ALS),[47] Alzheimer's,[48] and Parkinson's disease.[49] As the loss of BBLN-1 leads to IF aggregation, a potential future avenue of investigation is to examine whether BBLN-1 plays a direct role in protecting against protein aggregation.

STAR★METHODS

Detailed methods are provided in the online version of this paper and include the following:

- ● KEY RESOURCES TABLE
- ● RESOURCE AVAILABILITY
  - ○ Lead contact
  - ○ Materials availability
  - ○ Data and code availability
- ● EXPERIMENTAL MODEL AND SUBJECT DETAILS
  - ○ *Caenorhabditis elegans* strains and culture conditions
  - ○ Cell line culture
  - ○ Organoid culture
- ● METHOD DETAILS
  - ○ Isolation and initial mapping of mib41 and mib42
  - ○ Genomic DNA purification
  - ○ Identification of mib41 and mib42 mutations
  - ○ Protein structure and domain predictions
  - ○ Phylogenetic analysis
  - ○ Molecular cloning
  - ○ CRISPR/Cas9 genome engineering
  - ○ Light microscopy
  - ○ Texas Red-dextran assay
  - ○ FRAP experiments and analysis
  - ○ Feeding RNAi
  - ○ Electron microscopy
  - ○ Auxin Inducible Degradation
  - ○ Affinity-purification and mass spectrometry analysis
  - ○ Antibodies and Immunofluorescence Cell Staining
- ● QUANTIFICATION AND STATISTICAL ANALYSIS
  - ○ Image analysis
  - ○ Quantification of brood size and lethality
  - ○ Statistical analysis

SUPPLEMENTAL INFORMATION

Supplemental information can be found online at https://doi.org/10.1016/j.cub.2021.03.069.

AUTHOR CONTRIBUTIONS

DECLARATION OF INTERESTS

The authors declare no competing interests.

REFERENCES

1. Iruela-Arispe, M.L., and Beitel, G.J. (2013). Tubulogenesis. Development 140, 2851–2855.

2. Iruela-Arispe, M.L., and Davis, G.E. (2009). Cellular and molecular mechanisms of vascular lumen formation. Dev. Cell 16, 222–231.

3. Lubarsky, B., and Krasnow, M.A. (2003). Tube morphogenesis: making and shaping biological tubes. Cell 112, 19–28.

4. Sigurbjörnsdóttir, S., Mathew, R., and Leptin, M. (2014). Molecular mechanisms of de novo lumen formation. Nat. Rev. Mol. Cell Biol. 15, 665–676.

5. Sundaram, M.V., and Buechner, M. (2016). The *Caenorhabditis elegans* excretory system: a model for tubulogenesis, cell fate specification, and plasticity. Genetics 203, 35–63.

6. Sulston, J.E., Schierenberg, E., White, J.G., and Thomson, J.N. (1983). The embryonic cell lineage of the nematode *Caenorhabditis elegans*. Dev. Biol. 100, 64–119.

7. Leung, B., Hermann, G.J., and Priess, J.R. (1999). Organogenesis of the *Caenorhabditis elegans* intestine. Dev. Biol. 216, 114–134.

8. Pásti, G., and Labouesse, M. (2014). Epithelial junctions, cytoskeleton, and polarity. WormBook, 1–35.

9. Coch, R.A., and Leube, R.E. (2016). Intermediate filaments and polarization in the intestinal epithelium. Cells 5, 32.

10. Bossinger, O., Fukushige, T., Claeys, M., Borgonie, G., and McGhee, J.D. (2004). The apical disposition of the *Caenorhabditis elegans* intestinal terminal web is maintained by LET-413. Dev. Biol. 268, 448–456.

11. Munn, E.A., and Greenwood, C.A. (1984). The occurrence of submicrovillar endotube (modified terminal web) and associated cytoskeletal structures in the intestinal epithelia of nematodes. Philos. Trans. R. Soc. B Biol. Sci. 306, 1–18.

CellPress
OPEN ACCESS

12. Coulombe, P.A., and Wong, P. (2004). Cytoplasmic intermediate filaments revealed as dynamic and multipurpose scaffolds. Nat. Cell Biol. *6*, 699–706.

13. Etienne-Manneville, S. (2018). Cytoplasmic intermediate filaments in cell biology. Annu. Rev. Cell Dev. Biol. *34*, 1–28.

14. Geisler, F., and Leube, R.E. (2016). Epithelial intermediate filaments: guardians against microbial infection? Cells *5*, 29.

15. Salas, P.J., Forteza, R., and Mashukova, A. (2016). Multiple roles for keratin intermediate filaments in the regulation of epithelial barrier function and apico-basal polarity. Tissue Barriers *4*, e1178368.

16. Sanghvi-Shah, R., and Weber, G.F. (2017). Intermediate filaments at the junction of mechanotransduction, migration, and development. Front. Cell Dev. Biol. *5*, 81.

17. Toivola, D.M., Strnad, P., Habtezion, A., and Omary, M.B. (2010). Intermediate filaments take the heat as stress proteins. Trends Cell Biol. *20*, 79–91.

18. Carberry, K., Wiesenfahrt, T., Geisler, F., Stöcker, S., Gerhardus, H., Überbach, D., Davis, W., Jorgensen, E., Leube, R.E., and Bossinger, O. (2012). The novel intestinal filament organizer IFO-1 contributes to epithelial integrity in concert with ERM-1 and DLG-1. Development *139*, 1851–1862.

19. Geisler, F., Coch, R.A., Richardson, C., Goldberg, M., Bevilacqua, C., Prevedel, R., et al. (2020). Intestinal intermediate filament polypeptides in *C. elegans*: common and isotype-specific contributions to intestinal ultrastructure and function. Sci. Rep. *10*, 3142.

20. Geisler, F., Coch, R.A., Richardson, C., Goldberg, M., Denecke, B., Bossinger, O., and Leube, R.E. (2019). The intestinal intermediate filament network responds to and protects against microbial insults and toxins. Development *146*, dev169482.

21. Geisler, F., Gerhardus, H., Carberry, K., Davis, W., Jorgensen, E., Richardson, C., Bossinger, O., and Leube, R.E. (2016). A novel function for the MAP kinase SMA-5 in intestinal tube stability. Mol. Biol. Cell *27*, 3855–3868.

22. Davis, M.W., Hammarlund, M., Harrach, T., Hullett, P., Olsen, S., and Jorgensen, E.M. (2005). Rapid single nucleotide polymorphism mapping in *C. elegans*. BMC Genomics *6*, 118.

23. Joseph, B.B., Blouin, N.A., and Fay, D.S. (2018). Use of a sibling subtraction method for identifying causal mutations in *Caenorhabditis elegans* by whole-genome sequencing. G3 (Bethesda) *8*, 669–678.

24. Watanabe, N., Nagamatsu, Y., Gengyo-Ando, K., Mitani, S., and Ohshima, Y. (2005). Control of body size by SMA-5, a homolog of MAP kinase BMK1/ERK5, in *C. elegans*. Development *132*, 3175–3184.

25. Al-Hashimi, H., Hall, D.H., Ackley, B.D., Lundquist, E.A., and Buechner, M. (2018). Tubular excretory canal structure depends on intermediate filaments EXC-2 and IFA-4 in *Caenorhabditis elegans*. Genetics *210*, 637–652.

26. Khan, L.A., Jafari, G., Zhang, N., Membreno, E., Yan, S., Zhang, H., and Gobel, V. (2019). A tensile trilayered cytoskeletal endotube drives capillary-like lumenogenesis. J. Cell Biol. *218*, 2403–2424.

27. Karabinos, A., Schulze, E., Schünemann, J., Parry, D.A.D., and Weber, K. (2003). In vivo and in vitro evidence that the four essential intermediate filament (IF) proteins A1, A2, A3 and B1 of the nematode *Caenorhabditis elegans* form an obligate heteropolymeric IF system. J. Mol. Biol. *333*, 307–319.

28. Woo, W.-M., Goncharov, A., Jin, Y., and Chisholm, A.D. (2004). Intermediate filaments are required for *C. elegans* epidermal elongation. Dev. Biol. *267*, 216–229.

29. Bidaud-Meynard, A., Nicolle, O., Heck, M., Le Cunff, Y., and Michaux, G. (2019). A V0-ATPase-dependent apical trafficking pathway maintains the polarity of the intestinal absorptive membrane. Development *146*, dev174508.

30. Ramalho, J.J., Sepers, J.J., Nicolle, O., Schmidt, R., Cravo, J., Michaux, G., and Boxem, M. (2020). C-terminal phosphorylation modulates ERM-1 localization and dynamics to control cortical actin organization and support lumen formation during *Caenorhabditiselegans* development. Development *147*, dev188011.

31. Karabinos, A., Schünemann, J., and Weber, K. (2004). Most genes encoding cytoplasmic intermediate filament (IF) proteins of the nematode *Caenorhabditis elegans* are required in late embryogenesis. Eur. J. Cell Biol. *83*, 457–468.

32. Karabinos, A., Schulze, E., Klisch, T., Wang, J., and Weber, K. (2002). Expression profiles of the essential intermediate filament (IF) protein A2 and the IF protein C2 in the nematode *Caenorhabditis elegans*. Mech. Dev. *117*, 311–314.

33. Estes, K.A., Szumowski, S.C., and Troemel, E.R. (2011). Non-lytic, actin-based exit of intracellular parasites from *C. elegans* intestinal cells. PLoS Pathog. *7*, e1002227.

34. Stutz, K., Kaech, A., Aebi, M., Künzler, M., and Hengartner, M.O. (2015). Disruption of the *C. elegans* intestinal brush border by the fungal lectin CCL2 phenocopies dietary lectin toxicity in mammals. PLoS ONE *10*, e0129381.

35. Hüsken, K., Wiesenfahrt, T., Abraham, C., Windoffer, R., Bossinger, O., and Leube, R.E. (2008). Maintenance of the intestinal tube in *Caenorhabditis elegans*: the role of the intermediate filament protein IFC-2. Differentiation *76*, 881–896.

36. Nishimura, K., Fukagawa, T., Takisawa, H., Kakimoto, T., and Kanemaki, M. (2009). An auxin-based degron system for the rapid depletion of proteins in nonplant cells. Nat. Methods *6*, 917–922.

37. Zhang, L., Ward, J.D., Cheng, Z., and Dernburg, A.F. (2015). The auxin-inducible degradation (AID) system enables versatile conditional protein depletion in *C. elegans*. Development *142*, 4374–4384.

38. Potter, S.C., Luciani, A., Eddy, S.R., Park, Y., Lopez, R., and Finn, R.D. (2018). HMMER web server: 2018 update. Nucleic Acids Res. *46* (W1), W200–W204.

39. Schwarz, N., Windoffer, R., Magin, T.M., and Leube, R.E. (2015). Dissection of keratin network formation, turnover and reorganization in living murine embryos. Sci. Rep. *5*, 9007.

40. Asghar, M.N., Silvander, J.S.G., Helenius, T.O., Lähdeniemi, I.A.K., Alam, C., Fortelius, L.E., Holmsten, R.O., and Toivola, D.M. (2015). The amount of keratins matters for stress protection of the colonic epithelium. PLoS ONE *10*, e0127436.

41. Luck, K., Kim, D.-K., Lambourne, L., Spirohn, K., Begg, B.E., Bian, W., Brignall, R., Cafarelli, T., Campos-Laborie, F.J., Charloteaux, B., et al. (2020). A reference map of the human binary protein interactome. Nature *580*, 402–408.

42. Rolland, T., Taşan, M., Charloteaux, B., Pevzner, S.J., Zhong, Q., Sahni, N., Yi, S., Lemmens, I., Fontanillo, C., Mosca, R., et al. (2014). A proteome-scale map of the human interactome network. Cell *159*, 1212–1226.

43. Rual, J.-F., Venkatesan, K., Hao, T., Hirozane-Kishikawa, T., Dricot, A., Li, N., Berriz, G.F., Gibbons, F.D., Dreze, M., Ayivi-Guedehoussou, N., et al. (2005). Towards a proteome-scale map of the human protein-protein interaction network. Nature *437*, 1173–1178.

44. Paulson, C.C. (2009). Analysis of *C. elegans* genes required for maintaining intestinal lumen morphology and ingested drug resistance. PhD thesis (Southern Methodist University).

45. Shafaq-Zadah, M., Brocard, L., Solari, F., and Michaux, G. (2012). AP-1 is required for the maintenance of apico-basal polarity in the *C. elegans* intestine. Development *139*, 2061–2070.

46. Tsuboyama, K., Osaki, T., Matsuura-Suzuki, E., Kozuka-Hata, H., Okada, Y., Oyama, M., Ikeuchi, Y., Iwasaki, S., and Tomari, Y. (2020). A widespread family of heat-resistant obscure (Hero) proteins protect against protein instability and aggregation. PLoS Biol. *18*, e3000632.

47. Nijssen, J., Aguila, J., Hoogstraaten, R., Kee, N., and Hedlund, E. (2018). Axon-seq decodes the motor axon transcriptome and its modulation in response to ALS. Stem Cell Reports *11*, 1565–1578.

48. Kong, W., Mou, X., Liu, Q., Chen, Z., Vanderburg, C.R., Rogers, J.T., and Huang, X. (2009). Independent component analysis of Alzheimer's DNA microarray gene expression data. Mol. Neurodegener. *4*, 5.

49. Kim, S.M., Cho, S.Y., Kim, M.W., Roh, S.R., Shin, H.S., Suh, Y.H., Geum, D., and Lee, M.A. (2020). Genome-wide analysis identifies NURR1-controlled network of new synapse formation and cell cycle arrest in human neural stem cells. Mol. Cells *43*, 551–571.

50. Serra-Marques, A., Martin, M., Katrukha, E.A., Grigoriev, I., Peeters, C.A., Liu, Q., Hooikaas, P.J., Yao, Y., Solianova, V., Smal, I., et al. (2020). Concerted action of kinesins KIF5B and KIF13B promotes efficient secretory vesicle transport to microtubule plus ends. eLife *9*, e61302.

51. Wang, S., Wu, D., Quintin, S., Green, R.A., Cheerambathur, D.K., Ochoa, S.D., et al. (2015). NOCA-1 functions with γ-tubulin and in parallel to Patronin to assemble non-centrosomal microtubule arrays in *C. elegans*. eLife *4*, e08649.

52. Perez-Riverol, Y., Csordas, A., Bai, J., Bernal-Llinares, M., Hewapathirana, S., Kundu, D.J., Inuganti, A., Griss, J., Mayer, G., Eisenacher, M., et al. (2019). The PRIDE database and related tools and resources in 2019: improving support for quantification data. Nucleic Acids Res. *47* (D1), D442–D450.

53. Brenner, S. (1974). The genetics of *Caenorhabditis elegans*. Genetics *77*, 71–94.

54. Bolger, A.M., Lohse, M., and Usadel, B. (2014). Trimmomatic: a flexible trimmer for Illumina sequence data. Bioinformatics *30*, 2114–2120.

55. Cingolani, P., Platts, A., Wang, L., Coon, M., Nguyen, T., Wang, L., Land, S.J., Lu, X., and Ruden, D.M. (2012). A program for annotating and predicting the effects of single nucleotide polymorphisms, SnpEff: SNPs in the genome of Drosophila melanogaster strain w1118; iso-2; iso-3. Fly (Austin) *6*, 80–92.

56. Schwartz, M.L., and Jorgensen, E.M. (2016). SapTrap, a toolkit for high-throughput CRISPR/Cas9 gene modification in *Caenorhabditis elegans*. Genetics *202*, 1277–1288.

57. Dickinson, D.J., Slabodnick, M.M., Chen, A.H., and Goldstein, B. (2018). SapTrap assembly of repair templates for Cas9-triggered homologous recombination with a self-excising cassette. Micropubl. Biol. *2018*, https://doi.org/10.17912/W2KT0N.

58. Waaijers, S., Muñoz, J., Berends, C., Ramalho, J.J., Goerdayal, S.S., Low, T.Y., et al. (2016). A tissue-specific protein purification approach in *Caenorhabditis elegans* identifies novel interaction partners of DLG-1/Discs large. BMC Biol. *14*, 66.

59. Vicencio, J., Martínez-Fernández, C., Serrat, X., and Cerón, J. (2019). Efficient generation of endogenous fluorescent reporters by nested CRISPR in *Caenorhabditis elegans*. Genetics *211*, 1143–1154.

60. Arribere, J.A., Bell, R.T., Fu, B.X.H., Artiles, K.L., Hartman, P.S., and Fire, A.Z. (2014). Efficient marker-free recovery of custom genetic modifications with CRISPR/Cas9 in *Caenorhabditis elegans*. Genetics *198*, 837–846.

61. Ghanta, K.S., and Mello, C.C. (2020). Melting dsDNA donor molecules potentiates precision genome editing in *C. elegans*. bioRxiv. https://doi.org/10.1101/2020.08.03.235036.

62. Lamesch, P., Milstein, S., Hao, T., Rosenberg, J., Li, N., Sequerra, R., et al. (2004). *C. elegans* ORFeome version 3.1: increasing the coverage of ORFeome resources with improved gene predictions. Genome Res. *14* (10B), 2064–2069.

63. Kamath, R.S., Fraser, A.G., Dong, Y., Poulin, G., Durbin, R., Gotta, M., et al. (2003). Systematic functional analysis of the *Caenorhabditis elegans* genome using RNAi. Nature *421*, 231–237.

64. MacQueen, A.J., Baggett, J.J., Perumov, N., Bauer, R.A., Januszewski, T., Schriefer, L., et al. (2005). ACT-5 is an essential *Caenorhabditis elegans* actin required for intestinal microvilli formation. Mol. Biol. Cell *16*, 3247–3259.

65. Timmons, L., and Fire, A. (1998). Specific interference by ingested dsRNA. Nature *395*, 854.

66. McDonald, K.L. (2014). Rapid embedding methods into epoxy and LR White resins for morphological and immunological analysis of cryofixed biological specimens. Microsc. Microanal. *20*, 152–163.

67. Reipert, S., Goldammer, H., Richardson, C., Goldberg, M.W., Hawkins, T.J., Hollergschwandtner, E., Kaufmann, W.A., Antreich, S., and Stierhof, Y.-D. (2018). Agitation modules: flexible means to accelerate automated freeze substitution. J. Histochem. Cytochem. *66*, 903–921.

68. Mellacheruvu, D., Wright, Z., Couzens, A.L., Lambert, J.-P., St-Denis, N.A., Li, T., Miteva, Y.V., Hauri, S., Sardiu, M.E., Low, T.Y., et al. (2013). The CRAPome: a contaminant repository for affinity purification-mass spectrometry data. Nat. Methods *10*, 730–736.

69. Choi, H., Larsen, B., Lin, Z.-Y., Breitkreutz, A., Mellacheruvu, D., Fermin, D., Qin, Z.S., Tyers, M., Gingras, A.-C., and Nesvizhskii, A.I. (2011). SAINT: probabilistic scoring of affinity purification-mass spectrometry data. Nat. Methods *8*, 70–73.

70. van Ineveld, R.L., Ariese, H.C.R., Wehrens, E.J., Dekkers, J.F., and Rios, A.C. (2020). Single-cell resolution three-dimensional imaging of intact organoids. J. Vis. Exp. e60709.

STAR★METHODS

KEY RESOURCES TABLE

REAGENT or RESOURCE	SOURCE	IDENTIFIER
Antibodies		
Rabbit anti-BBLN	Sigma-Aldrich	Cat# HPA020725; RRID: AB_1845816
Mouse anti-PCNT	Abcam	Cat# ab28144; RRID: AB_2160664
Rat anti-Tyrosinated α-tubulin (YL1/2)	Thermo Fisher Scientific	Cat# MA1-80017; RRID: AB_2210201
Rat anti-KRT8	DSHB	Cat# TROMA-I; RRID: AB_531826
Alexa Fluor 568-conjugated Phalloidin	Life Technologies	Cat# A12380
Goat anti-mouse Alexa Fluor 488	Life Technologies	Cat# A11029; RRID: AB_2534088
Goat anti-rabbit Alexa Fluor 594	Thermo Fisher Scientific	Cat# A-11012; RRID AB_2534079
Goat anti-rat Alexa Fluor 647	Thermo Fisher Scientific	Cat# A-21247; RRID AB_141778
Rabbit anti-GFP	Abcam	Cat# AB290; RRID: AB_2313768
Goat anti-rabbit IgG Antibody, IRDye 680LT Conjugated	LI-COR Biosciences	Cat# 827-11081; RRID: AB_10795015
Goat anti-rat IgG Antibody, IRDye 800CW Conjugated	LI-COR Biosciences	Cat# 926-32219; RRID: AB_1850025
Bacterial and virus strains		
E. coli OP50	CGC	N/A
E. coli DH5a	Thermo Fisher Scientific	Cat# 18265017
E. coli HT115	CGC	N/A
Vidal full-length HT115 RNAi feeding library	SourceBioScience	3320_Cel_ORF_RNAi
Ahringer fragment HT115 RNAi feeding library	SourceBioScience	3318_Cel_RNAi_complete
Chemicals, peptides, and recombinant proteins		
Vectashield mounting medium with DAPI	Vector Laboratories	Cat# H-1200
PEI	PolySciences	Cat# 24765–2
cOmplete, EDTA-free Protease Inhibitor Cocktail	Roche	Cat# 4693116001
Dextran, Texas Red, 3000 MW	Thermo Fisher Scientific	Cat# D3329
Dextran, Texas Red, 10,000 MW	Thermo Fisher Scientific	Cat# D1828
Dextran, Texas Red, 40,000 MW	Thermo Fisher Scientific	Cat# D1829
Alt-R S.p. Cas9 Nuclease V3	IDT	Cat# 1081058
Auxin	Alfa Aesar	Cat# A10556
Critical commercial assays		
MinElute PCR purification kit	QIAGEN	28004
Dynabeads M-280 streptavidin beads	Thermo Fisher	Cat# 11206D
Deposited data		
Mass Spectrometry data	PRIDE	PXD024387
Experimental models: cell lines		
Human embryonic kidney 239T (HEK293T)	ATCC	Cat# CRL-3216
HeLa (Kyoto)	Serra-Marques et al.[50]	N/A
Mouse C57BL/6 small intestine organoids; isolated from duodenum.	This study	N/A
Experimental models: organisms/strains		
wild type (Bristol)	CGC	N2
mibIs39[Prps-27::GFP-2xTEV-Avi 10 ng/ul + Prab-3::mCherry 5 ng/ul + lambda DNA 65 ng/ul] I	This study	BOX64
erm-1(mib15[erm-1::eGFP]) I	Ramalho et al.[30]	BOX213
erm-1(mib15[erm-1::eGFP]) I; sma-5a(mib41[C370T]) X	This study	BOX320

(Continued on next page)

Continued

REAGENT or RESOURCE	SOURCE	IDENTIFIER
erm-1(mib15[erm-1::eGFP]) I; bbln-1(mib42[C13T]) X	This study	BOX321
bbln-1(mib71[eGFP::bbln-1]) X	This study	BOX414
bbln-1(mib79[bbln-1::mkate2(co)]) X	This study	BOX459
erm-1(mib40[erm-1::AID::mCherry]) I; bbln-1(mib70 [Pbbln-1::eGFP1-3, X:3151104..3153328]) X	This study	BOX415
erm-1(mib40[erm-1::AID::mCherry]) I; bbln-1(mib71 [eGFP::bbln-1]) X	This study	BOX427
ifb-2(mib74[ifb-2::mCherry]) II; bbln-1(mib70[Pbbln-1::eGFP1-3, X:3151104..3153328]) X	This study	BOX435
ifb-2(mib74[ifb-2::mCherry]) II; bbln-1(mib71[eGFP::bbln-1]) X	This study	BOX436
erm-1(mib15[erm-1::eGFP]) I; ifb-2(mib74[ifb-2::mCherry]) II	This study	BOX514
erm-1(mib15[erm-1::eGFP]) I; ifb-2(mib74[ifb-2::mCherry]) II; bbln-1(mib70[Pbbln-1::eGFP1-3, X:3151104..3153328]) X	This study	BOX515
erm-1(mib40[erm-1::AID::mCherry]) I	This study	BOX303
erm-1(mib40[erm-1::AID::mCherry]) I; bbln-1(mib42 [C13T]) X	This study	BOX330
erm-1(mib15[erm-1::eGFP]) I; bbln-1(mib42[Q5STOP]) X; dlg-1(mib23[dlg-1::mCherry-LoxP]) X	This study	BOX307
erm-1(mib15[erm-1::eGFP]) I; dlg-1(mib23[dlg-1::mCherry-LoxP]) X	This study	BOX368
nrfl-1(mib72[nrfl-1::mCherry]) IV	Boxem lab	BOX416
ifb-2(mib74[ifb-2::mCherry]) II; bbln-1(mib70[Pbbln-1::eGFP1-3, X:3151104..3153328]) X; dlg-1(mib35[dlg-1::AID::eGFP-LoxP]) X	This study	BOX454
ifb-2(mib74[ifb-2::mCherry]) II; dlg-1(mib35[dlg-1::AID::eGFP-LoxP]) X	This study	BOX455
erm-1(mib40[erm-1::AID::mCherry])I; ifc-2a::yfp(kc16)X	This study	BOX456
erm-1(mib40[erm-1::AID::mCherry]) I; ifc-2a::yfp(kc16) X; bbln-1(mib70[Pbbln-1::eGFP1-3, X:3151104..3153328]) X	This study	BOX457
erm-1(mib40[erm-1::AID::mCherry]) I; ifd-2(mib94 [eGFP::ifd-2]) X	This study	BOX614
erm-1(mib40[erm-1::AID::mCherry]) I; ifd-2(mib94 [eGFP::ifd-2]) X; bbln-1(mib70[Pbbln-1::eGFP1-3, X:3151104..3153328]) X	This study	BOX615
Is[Pges-1::YFP::ACT-5]	Bossinger et al.[10]	JM125
bbln-1(mib70[Pbbln-1::eGFP1-3, X:3151104..3153328]) X; Is[Pges-1::YFP::ACT-5]	This study	BOX438
par-6(mib24[par-6::eGFP-LoxP]) I; let-413(mib29[let-413::mCherry-LoxP]) V	Boxem lab	BOX251
gip-2(lt19[gip-2::GFP]::loxP::cb-unc-119(+)::loxP) I; bbln-1(mib93[mCherry::bbln-1]) X	This study	BOX544
mibIs48[Pelt-2::TIR-1::tagBFP2-Lox511::tbb-2-3′UTR, IV:5014740-5014802 (cxTi10882 site)]) IV; bbln-1(mib111 [eGFP::AID::bbln-1]) X	This study	BOX632
erm-1(mib15)I; IFB-2(mib74[IFB-2::mCherry]) II; mibIs48 [Pelt-2::TIR-1::tagBFP2-Lox511::tbb-2-3′UTR, IV:5014740-5014802 (cxTi10882 site)]) IV; bbln-1(mib111 [GFP::AID::BBLN-1]) X	This study	BOX637
erm-1(mib40[erm-1::AID::mCherry]) I; ifb-2(kc14) II; bbln-1(mib70[Pbbln-1::eGFP1-3, X:3151104..3153328]) X	This study	BJ364

Continued

REAGENT or RESOURCE	SOURCE	IDENTIFIER
gip-2(lt19[gip-2::GFP]::loxP::cb-unc-119(+)::loxP)I; unc-119(ed3)III	Wang et al.[51]	OD2509
ifb-1(mib134[ifb-1::mCherry]) II	This study	BOX717
ifb-1(mib134[ifb-1::mCherry]) II; bbln-1(mib70[Pbbln-1::eGFP1-3, X:3151104..3153328])X	This study	BOX724
ifb-1(mib134[ifb-1::mCherry]) II; bbln-1(mib71[GFP::bbln-1])X	This study	BOX725
Oligonucleotides		
See Table S1.	N/A	N/A
Recombinant DNA		
Pvha-6::gfp::bbln-1::N-taglinker::tbb-2_3'UTR	This study	pSMR10
vha-6 promoter	This study	pSMR13
tbb-2 3'UTR	This study	pSMR18
Pvha-6::gfp::BBLN (Hs)::N-taglinker::tbb-2_3'UTR	This study	pSMR30
act-5 3'UTR (L4440)	This study	pSMR33
ifp-1 (L4440)	This study	pSMR34
ifd-1 (L4440)	This study	pSMR35
ifo-1 (L4440)	This study	pSMR36
L4440	Addgene	Cat# 1654
pHSG298	Takara Biosciences	Cat# 3298
pMLS257	Addgene	Cat# 73716
pMLS288	Addgene	Cat# 73735
pMLS287	Addgene	Cat# 73730
pDD363	Addgene	Cat# 91829
pDD398	Addgene	Cat# 91832
Peft-3::Cas9	Addgene	Cat# 46168
Pmyo-2::mCherry	Addgene	Cat# 19327
pJJR82	Addgene	Cat# 75027
pJJR83	Addgene	Cat# 75028
Software and algorithms		
ImageJ	Rasband,W.S (NIH)	RRID: SCR_003070
Graphpad Prism	GraphPad	RRID: SCR_002798
Zen Black	Zeiss	RRID: SCR_018163
SnapGene	Insightful Science	RRID: SCR_015052
Proteome Discoverer 1.4	Thermo Scientific	RRID: SCR_014477

RESOURCE AVAILABILITY

Lead contact
Further information and requests for resources and reagents should be directed to and will be fulfilled by the Lead Contact, Mike Boxem (m.boxem@uu.nl).

Materials availability
Plasmids and *C. elegans* strains generated in this study are available upon request made to the Lead Contact.

Data and code availability
The mass spectrometry proteomics data have been deposited to the ProteomeXchange Consortium via the PRIDE partner repository.[52] The accession number for the proteomics data is PRIDE: PXD024387.

EXPERIMENTAL MODEL AND SUBJECT DETAILS

Caenorhabditis elegans strains and culture conditions

Caenorhabditis elegans strains were cultured on standard nematode growth medium (NGM) agar plates at 15 or 20°C and fed with *Escherichia coli* OP50.[53] The Key resources table contains a list of all the strains used. Transgenic lines were generated by injecting 15 ng/μl of either plasmid pSMR10 or pSMR30 together with 65 ng/μl lambda DNA (Thermo Scientific) into the gonads of young adults.

Cell line culture

HeLa and HEK293T cell lines were cultured in DMEM/Ham's F10 (50:50) supplemented with 10% FCS and 1% penicillin/streptomycin at 37 °C and 5% CO2. All cell lines routinely tested negative for mycoplasma.

Organoid culture

Mouse small intestinal organoids derived from the duodenum of C57BL/6 mice were cultured in ENR medium: Advanced DMEM/F12 (Invitrogen) with 1% Penicillin/Streptomycin (P/S, Lonza), 1% HEPES buffer (Invitrogen) and 1% Glutamax (Invitrogen), supplemented with 5% R-spondin conditioned medium, 10% Noggin conditioned medium, 50 ng/ml EGF (Invitrogen), 1x B27 (Invitrogen), 1.25 mM n-Acetyl Cysteine (Sigma-Aldrich).

METHOD DETAILS

Isolation and initial mapping of mib41 and mib42

L4 stage *erm-1::GFP* animals were incubated for 6 hours at room temperature (RT) in M9 buffer (0.22 M KH_2PO_4, 0.42 M Na_2HPO_4, 0.85 M NaCl, 0.001 M $MgSO_4$) supplemented with 50 mM ethyl methanesulfonate (EMS), in a 15 mL tube with gentle rotation. Mutagenized L4 animals were placed on 9 cm NGM agar plates seeded with *E. coli* (35 plates, 10 animals per plate) and allowed to lay eggs. Parents were removed after ~1000 F1 progeny had been produced. Three days after F1 progeny started egg-laying, all F1 adults and L2 larvae were washed off the plate, leaving behind a semi-synchronous population of F2 embryos. F2 animals were allowed to develop for 2–4 days at 20°C and scored for intestinal morphology defects using a Leica MZ16 fluorescence stereoscope. Two mutants, *mib41* and *mib42*, were isolated and backcrossed with N2 males 3 times before further analysis. To identify an approximate genetic location for both mutations, single-nucleotide polymorphism (SNP) mapping using the polymorphic strain CB4856 was performed as described previously.[22]

Genomic DNA purification

C. elegans lysis and genomic DNA purification were performed using the DNeasy Blood and Tissue kit (QIAGEN). Animals from two recently starved populations were collected, pooled, washed twice using M9, and resuspended in 400 μL of lysis (ATL) buffer. Samples were then flash-frozen in liquid nitrogen and stored overnight at −80°C. After three rounds of liquid nitrogen freeze-thawing, proteinase K was added to a final concentration of 2 mg/ml and samples were incubated for 3 hours at 56°C while shaking at 600 rpm. Samples were further incubated with 2 mg/ml RNase A for 30 min at RT and for 10 min at 56°C after addition of 400 μL of AL buffer. Finally, samples were mixed with 400 μL of 100% ethanol and loaded into purification columns. Wash and elution steps were performed according to the manufacturer's instructions. Concentration of genomic DNA samples was measured using Qubit Fluorometric Quantification (Invitrogen).

Identification of mib41 and mib42 mutations

We used the sibling subtraction method to identify the causative *mib41* and *mib42* mutations by whole-genome sequencing (WGS).[23] From heterozygous *erm-1::GFP/+; mib41/+* or *erm-1::GFP/+; mib42/+* hermaphrodites we isolated homozygous *mib41* or *mib42* mutant, homozygous nonmutant, or heterozygous F2 progeny. Genomic DNA was then purified from pooled F3 progeny derived from 12–16 F2 animals and sequenced on an Illumina HiSeq X Ten platform.

To prepare the raw sequence data (provided in FASTQ format) for variant analysis, we first removed adapters and low quality leading or trailing bases using Trimmomatic version 0.38:[54] *java -jar trimmomatic-0.35.jar PE input_forward.fq.gz input_reverse.fq.gz output_forward_paired.fq.gz output_forward_unpaired.fq.gz output_reverse_paired.fq.gz output_reverse_unpaired.fq.gz ILLUMINACLIP:TruSeq3-PE-2.fa:2:30:10 LEADING:3 TRAILING:3 SLIDINGWINDOW:4:15 MINLEN:36*.

Next, reads were aligned to the *C. elegans* reference genome (UCSC genome release ce11) using the Burrows-Wheeler Aligner version 0.7.17 BWA-MEM algorithm (http://bio-bwa.sourceforge.net): *bwa mem -M ce11.fa read1.fq read2.fq > output.sam*.

Third, non-aligned pairs were removed using the sam_bitwise_flag_filter.py script from the Galaxy project (https://galaxyproject.org): *python sam_bitwise_flag_filter.py -f input.sam–flag_column 2 '–0x0001 = 1' '–0x0002 = 1' > output.sam*.

Fourth, Picard tools version 2.18.14 (http://broadinstitute.github.io/picard/) and Samtools version 1.9 (http://www.htslib.org/) were used to convert the Sequence Alignment Map (SAM) file into a variant analysis-ready Binary Alignment Map (BAM). A sequence dictionary file was created for the *C. elegans* reference genome (*java -jar picard.jar CreateSequenceDictionary -O ce11.dict -R ce11.fa*) and added to the SAM file (*cat ce11.dict aligned_reads.sam > output.sam*). The SAM file was then sorted by coordinate (*java -jar picard.jar SortSam -I input.sam -O output.sam -SO coordinate*), read group names were added and the file converted to BAM format

(java -jar picard.jar AddOrReplaceReadGroups -I input.sam -O output.bam -RGID rgid -RGLB lib1 -RGPL illumina -RGPU unit1 -RGSM sample_name -SORT_ORDER coordinate).

Finally, duplicate reads were marked (java -jar picard.jar MarkDuplicates -I input.bam -O output.bam -M metrics.txt -REMOVE_DUPLICATES true -ASSUME_SORT_ORDER coordinate) and the BAM file was indexed (bamtools index -in input.bam).

Variant discovery was performed using the Genome Analysis Toolkit (GATK version 4.0.9.0) (https://gatk.broadinstitute.org/hc). First, variants were called per-sample using HaplotypeCaller in genomic variant call format (gVCF) mode: *gatk HaplotypeCaller -R ce11.fa -I input.bam O output.g.vcf.gz -ERC GVCF*. Next, per-sample gVCF files (mutant, heterozygous, and wild-type pools for both mutants) were combined into a multi-sample gVCF file: *gatk CombineGVCFs -R ce11.fasta -V input1.g.vcf.gz -V input2.g.vcf.gz (etc) -O output.g.vcf.gz*. Finally, joint genotyping was performed on the combined gVCF file: *gatk GenotypeGVCFs -R ce11.fasta -V input.g.vcf.gz -O output.vcf.*.

To identify candidate causative mutations, we first added genomic variant annotations and functional effect predictions to the VCF file using SnpEff (Version 4.3T with annotation file WBcel235.86):[55] *java -jar snpEff.jar WBcel235.86 input.vcf. > output.vcf.*. The relevant data was then exported to a tab-delimited table using GATK: *gatk VariantsToTable -R ce11.fa -F CHROM -F POS -GF AD -F ANN -O output.tab*. This exports the chromosome, position, allelic depth (the number of reads corresponding to the reference and that are variant), and the annotation.

Final analysis was done in Microsoft Excel, by selecting variants present at a frequency > 0.8 in the homozygous mutant sample, < 0.8 in the heterozygous sample, and < 0.1 in the homozygous wild-type sample. For both mutant alleles, only a single variant from the resulting selection was predicted to affect a protein coding sequence, which was selected for further analysis.

Protein structure and domain predictions
General protein domain searches were done using the SMART service at http://smart.embl-heidelberg.de/. Coiled-coils predictions were done using DeepCoil at https://toolkit.tuebingen.mpg.de/#/tools/deepcoil. Disorder predictions were done using DisEMBL at http://dis.embl.de/. Default settings were used. EMBOSS Water analysis was used to calculate similarity between BBLN-1 and bublin.

Phylogenetic analysis
To identify proteins related to C15C7.5/BBLN-1, we performed a three-iteration HMMER search against the Reference Proteomes dataset at https://www.ebi.ac.uk/Tools/hmmer/.

Molecular cloning
SapTrap assembly was done as described[56] using existing SEC donor modules[57] or new donor modules generated by cloning PCR fragments or custom gBlocks (IDT) into Eco53kI-digested vector pHSG298 (Takara Biosciences). For the *Pvha-6::GFP::bbln-1::tbb-2 3'UTR* and *Pvha-6::GFP::bublin (Hs)::tbb-2 3'UTR* rescue constructs, *Pvha-6* was amplified from genomic N2 DNA, *GFP* and the *tbb-2 3'UTR* were amplified from prior plasmids, and the *bbln-1* and *bublin* sequences were synthesized as gBlocks (IDT). GFP sequence is codon-optimized and contains 3 artificial introns. A list of all used oligonucleotides (IDT) and gBlocks (IDT) is included in Table S1 and used plasmids are listed in the Key resources table. PCR fragments were generated using Q5 Hot Start High-Fidelity DNA Polymerase (New England Biolabs). All DNA vectors used for genome editing were purified from DH5α *E. coli* using a QIAGEN midiprep kit. Annotated DNA files of all plasmids used are included as Methods S1.

CRISPR/Cas9 genome engineering
Endogenous gene fusions were generated in an N2 background by homology-directed repair of CRISPR/Cas9-induced DNA double-strand breaks (DSBs). Microinjection of young adult hermaphrodite germlines was done using an inverted microinjection setup (Eppendorf FemtoJet 4x mounted on a Zeiss Axio Observer A.1 equipped with an Eppendorf Transferman 4r). In cases where the sgRNA target site was not disrupted by sequence integration, silent mutations were incorporated to prevent repeated DNA cleavage. In all cases correct integration was confirmed by Sanger sequencing (Macrogen). A list of all DNA- and RNA-based reagents is included as Table S1.

erm-1::mCherry was generated using the SEC method, using a plasmid-based repair template. sgRNA expression plasmids were generated by ligating annealed oligo pairs into BbsI-digested pJJR50 as previously described.[58] The repair template was assembled into pMLS257 using SapTrap with custom and SEC modules as follows (from 5' to 3'): left homology arm, a C-terminal linker (pMLS287), mCherry, SEC (pDD363), auxin-inducible degron (AID; pDD398), and right homology arm. Homology arms of ~600 bp upstream and downstream of the DSB were amplified from N2 genomic DNA. The injection mix contained: 60 ng/μl *Peft-3::Cas9* (Addgene #46168), 15 ng/μl repair template, 100 ng/μl for each sgRNA, and 2.5 ng/μl *Pmyo-2::mCherry* (Addgene #19327). Three injected animals were pooled and incubated for 3 days at 20°C before adding 250 ng/μl of hygromycin per plate. Rol animals lacking visible mCherry expression were selected after 4–5 days. To eliminate the selection cassette through Cre-Lox recombination, L1 progeny of selected homozygous Rol animals were heat-shocked in a water bath at 34°C for 1 hour. Correct excision was confirmed by selection of non-Rol animals and subsequent Sanger sequencing. Sequence files of the final gene fusions are included in Methods S1.

The *bbln-1(mib70)*, *GFP::bbln-1*, and *ifb-2::mCherry* alleles were generated using the plasmid-free nested-CRISPR approach.[59] Injection mixes contained the following reagents (IDT): 250 ng/μl Alt-R S.p. Cas9 Nuclease V3 (IDT), 2 μM step 1 ssODN repair

template, 400 ng/μl step 2 PCR repair template, 4.5-5 μM step 1 and step 2 crRNAs, 10 μM tracrRNA, as well as 1 μM *dpy-10* crRNA and ssODN repair for co-CRISPR selection.[60] Reagents for *dpy-10* co-CRISPR selection were omitted in *ifb-2::mCherry* injection mixes, and for *bbln-1(mib70)* only step 1 editing events were selected. To select for integration events, injected animals were transferred to individual plates and allowed to recover at 20°C overnight before incubation at 25°C for 2–3 days. F1 animals were either visually screened for presence of fluorescence using a Leica MZ16 fluorescence stereomicroscope, or singled from plates with high numbers of Dpy and Rol animals followed by PCR screening.

All other strains were produced using a plasmid-free protocol incorporating melting of double stranded DNA (dsDNA) repair templates.[61] Selection of positive editing events was done by visually screening for expression of fluorescent protein, or by PCR analysis of single animals from plates with high numbers of Rol animals.

Light microscopy

Imaging of *C. elegans* was done by mounting embryos or larvae on a 5% agarose pad in a 10 mM Tetramisole solution in M9 buffer to induce paralysis. Spinning disk confocal imaging was performed using a Nikon Ti-U microscope equipped with a Yokogawa CSU-X1-M1 confocal head and an Andor iXon DU-885 camera, using a 60x 1.4 NA objective. Time-lapse imaging for FRAP experiments was performed on a Nikon Eclipse-Ti microscope equipped with a Yokogawa CSU-X1-A1 spinning disk and a Photometrics Evolve 512 EMCCD camera, using a 100x 1.4 NA objective. Targeted photobleaching was done using an ILas system (Roper Scientific France/ PICT-IBiSA, Institut Curie). Point-scanning confocal microscopy was done on a Zeiss AiryScan LSM 880 setup using a Plan-Apochromat 63x 1.2 NA objective. bublin antibody test was imaged on an upright fluorescence Nikon Eclipse Ni-U microscope using a Plan Apo Lambda 100x N.A. 1.45 oil objective. Confocal imaging for keratin 8 and bublin in HeLa cells was performed with Leica TCS SP8 STED 3X microscope using HC PL APO 100x/1.4 oil STED WHITE objective driven by LAS X controlling software. Microscopy data was acquired using MetaMorph Microscopy Automation & Image Analysis Software (Spinning Disk), and Zen Black software (AiryScan). All stacks along the z axis were obtained at 0.25 μm intervals. For quantifications, the same laser power and exposure times were used within experiments.

Texas Red-dextran assay

Mixed-stage populations were collected in egg buffer (118 mM NaCl, 48 mM KCl, 2 mM MgCl$_2$, 2 mM CaCl$_2$, 25 mM HEPES pH 7.3) and washed three times. The worm pellet was concentrated and resuspended in a solution containing 1 mg/ml Texas Red-dextran. The samples were incubated for 90 min while shaking at 300 rpm in the dark. The dye in solution was removed by washing the samples with egg buffer until the solution was clear, and animals were either imaged directly or transferred to standard culture plates for 1 hour prior to imaging. Animals were paralyzed in 10 mM Tetramisole, transferred to a 5% agarose pad on a glass slide, and imaged by spinning disk confocal microscopy.

FRAP experiments and analysis

For FRAP assays, laser power was adjusted in each experiment to avoid complete photobleaching of the selected area. Photobleaching was performed on a circular region with a diameter of 30 or 40 px (respectively 3.33 or 4.44 μm) at the cortex, and recovery was followed at 5 s intervals for 15 minutes. Time-lapse movies were analyzed in ImageJ. The size of the area for FRAP analysis was defined by the full width at half-maximum of an intensity plot across the bleached region in the first post-bleach frame. For each time-lapse frame, the mean intensity value within the bleached region was determined, and the background, defined as the mean intensity of a non-bleached region outside the animal, was subtracted. The mean intensities within the bleached region were corrected for acquisition photobleaching per frame using the background-subtracted mean intensity of a similar non-bleached region at the cortex, which was normalized to the corresponding pre-bleach mean intensity. FRAP recovery was calculated as the change in corrected intensity values within the bleached region. The first frame after bleach was defined as 0, and the mean intensity of the 10 frames before bleach as 1.

Curve fitting was done using GraphPad Prism 8, on averaged recovery data per sample using non-linear regression analysis (least-squares regression). One and two-phase association were tested and, in all cases, data were best fitted with a two-phase curve.

Feeding RNAi

RNAi clones for *bbln-1*, *ifb-2*, *ifc-2* and *ifd-2* were obtained from the genome wide Vidal full-length HT115 RNAi feeding library derived from the ORFeome 3.1 collection.[62] The RNAi clone for *ifc-1* was obtained from the genome wide Ahringer fragment HT115 RNAi feeding library,[63] supplied through Source BioScience. All clones were verified using Sanger sequencing. RNAi clones for *ifo-1*, *ifd-1*, *ifp-1, let-413* and *sma-5* were generated by subcloning the corresponding cDNA into a modified L4440 RNAi feeding vector, containing a linker with AscI and NotI restriction sites. To specifically target *act-5*, and no other actin isoforms that share extensive sequence homology, we followed a previously described strategy and designed an RNAi clone against the unique 3′UTR.[64] For all custom RNAi clones, fragments were amplified from a cDNA library, digested with AscI/NotI, ligated into AscI/NotI-digested L4440, and transformed into *E. coli* DH5α. Single colonies were isolated, plasmid DNA was purified, and presence of an insert was confirmed by Sanger sequencing. Correct clones were re-transformed into *E. coli* HT115, again confirmed by sequencing and stored at −80°C in 50% glycerol (1:1). All primer pairs are listed in Table S1.

For feeding RNAi experiments, bacterial clones were pre-cultured in 2 mL Lysogeny Broth (LB) supplemented with 100 μg/ml ampicillin and 2.5 μg/ml tetracycline at 37°C while rotating at 200 rpm for 6–8 hours, and then transferred to new tubes with a total volume

of 10 mL and cultured overnight. An HT115 bacterial clone expressing the L4440 vector lacking an insert was used as a control in feeding experiments. To induce production of dsRNA, cultures were incubated for 90 min in the presence of 1 mM Isopropyl β-D-1-thiogalactopyranoside (IPTG). Bacterial cultures were pelleted by centrifugation at 3220 g for 15 min and concentrated 5x. NGM agar plates supplemented with 100 μg/ml ampicillin and 1 mM IPTG were seeded with 250 μL of bacterial suspension, and kept at room temperature for 48 hour in the dark. L1 or L4 hermaphrodites were placed on the seeded RNAi plates and incubated at 20°C.[65]

Electron microscopy
Young adult animals were transferred into a 100 μm deep membrane carrier containing 20% bovine serum albumin in M9 worm buffer (22 mM KH_2PO_4, 42 mM Na_2HPO_4, 86 mM NaCl, 1 mM $MgSO_4$) and then high-pressure frozen in a Leica EM Pact high-pressure freezer. A minimum of five samples with 10-20 animals were frozen per experiment. Quick freeze substitution with agitation using 1% OsO_4, 0.2% uranyl acetate in acetone followed by rapid epoxy resin embedding was performed as previously described.[66,67] Subsequently, 50 nm thick sections of the embedded samples were prepared using a Leica UC7. These were contrasted for 10 min in 1% uranyl acetate in ethanol and Reynolds lead citrate and recorded at 100 kV on a Hitachi H-7600 transmission electron microscope (Tokyo, Japan).

Auxin Inducible Degradation
Auxin treatment was performed by transferring worms to NGM plates seeded with *E. coli* OP50 and containing 1 mM auxin. To pre-pare plates, auxin was added to the autoclaved NGM agar medium after cooling to 60°C prior to plate pouring. Plates were kept for a maximum of 2 weeks in the dark at 4°C. 40 adults were placed on NGM plates seeded with *E. coli* OP50 and allowed to lay eggs. After 1 hour of egg laying, plates were washed with M9 (0.22 M KH2 PO4, 0.42 M Na2 HPO4, 0.85 M NaCl, 0.001 M MgSO4) buffer to remove larvae and adults. For the auxin withdrawal experiments, additional synchronization was performed by washing the plates with M9 again after 1 h, to collect larvae hatched within that time span.

Affinity-purification and mass spectrometry analysis
GFP pull-down from C. elegans
Animals endogenously expressing GFP-tagged BBLN-1 or control animals expressing an integrated GFP transgene[58] were grown on 6–8 9 cm NGM plates until starvation, to enrich for L1 animals. Animals were then transferred into 250 mL of S-Medium supplemented with 1% Penn/Strep (Life Technologies), 0.1% nystatin (Sigma) and OP50 bacteria obtained from the growth of a 400 mL culture. Animals were grown at 20°C at low shaking for 96 hours and were harvested and cleaned using a sucrose gradient, as previously described[58] with one exception being the inclusion of $MgSO_4$ in the M9 medium. Worms were distributed into 15 mL TPX tubes (Diagenode) to reach 200–400 μl worm pellet per tube and were washed with lysis buffer (25mM Tris-HCl pH 7.5, 150mM NaCl, 1mM EDTA, 0.5% IGEPAL CA-630, 1X cOmplete Protease Inhibitor Cocktail (Roche)). The liquid was removed, and the sample was flash frozen in liquid nitrogen for storage at −80°C.

To lyse the worms, tubes were thawed on ice and ice-cold lysis buffer was added to reach a total volume of 2 ml. Tubes were son-icated for 10 mins (sonication cycle: 30 s ON, 30 s OFF) at 4°C in a Bioruptor ultrasonication bath (Diagenode) at high energy setting. After lysis, lysates were cleared by centrifugation and protein levels were measured using the Bradford BCA assay (Thermo Scientific).

Immunoprecipitation was performed using GFP-Trap Magnetic Agarose beads (Chromotek) according to manufacturer's protocol, using 25 μl of beads per sample. To prep the beads, they were first equilibrated in wash buffer (10 mM Tris/Cl pH 7.5, 150 mM NaCl, 0.5 mM EDTA, 0.1% IGEPAL CA-630), blocked with 1% BSA for 1 hour, then washed 4 times with wash buffer. Next, lysate was added to the beads and they were incubated for 1 hour tumbling end-over-end. Lysate was then removed, and the beads were washed 4 times in wash buffer. After the final wash step, all liquid was removed, and the beads were flash frozen with liquid nitrogen. The experiment was performed in triplicate (biological replicates) and processed on independent days.

Biotin-streptavidin pull-down from cells
Confluent HEK293T cells were split in a 1:3 dilution 24 hours before transfection. Cells were transfected with overexpression con-structs indicated in figure legend together with BirA. 1 μg/μL PEI (Polyethylenimine HCl MAX Linear MW 40000 (PolySciences, 24765–2)) and 1 μg/μL DNA (3:1) were mixed in Ham's F10 and incubated for 5 minutes at room temperature. The mixture was added to cells and incubated for 24 hours to allow expression. The cells were harvested in ice-cold PBS and lysed with lysis buffer (150 mM Tris-HCl pH 7.5, 150 mM NaCl, 1% Triton X-100 and cOmplete protease inhibitor cocktail (Roche)). 90% of each cell lysate was centrifuged at 13,000 rpm for 5 minutes and the supernatants were transferred and incubated with streptavidin beads (Dynabeads M-280, Invitrogen), which were already blocked by 0.2% Chicken Egg Albumine (Sigma). The remaining cell lysates were denatured with SDS/DTT sample buffer and used as input sample. Beads were incubated for 40 minutes at 4°C, before washing 5 times with washing buffer (100mM Tris pH7.5, 150 mM NaCl, 0.5% Triton X-100 and 0.5x protease inhibitor cocktail).

Western blot analysis for bublin/keratin pull-down
For western blot assays, pull-down samples were eluted with SDS/DTT sample buffer and boiled for 5 min at 95°C. Both pull-down and input were loaded into 10% SDS-PAGE gels and transferred to nitrocellulose membrane. Membranes were blocked with 2% BSA (bovine serum albumin) in PBS/0.05% Tween-20. Primary antibodies were diluted in blocking buffer and incubated with the membranes overnight at 4°C, washed 3 times with PBS/0.05% Tween-20 and incubated with IRDye 680LT and IRDye 800CW

antibodies (LI-COR Biosciences) for 45 min at RT. Membranes were washed 3 times with PBS/0.05% Tween-20 before imaging on an Odyssey Infrared Imaging system (LI-COR Biosciences).

Mass spectrometry analysis for BBLN-1/bublin

Streptavidin and anti-GFP beads after affinity purification were resuspended in 15 μL of 4 × Laemmli sample buffer (Biorad), boiled at 99°C for 10 min and supernatants were loaded on 4%–12% Criterion XT Bis–Tris precast gel (Biorad). The gel was fixed with 40% methanol and 10% acetic acid and then stained for 1 hour using colloidal Coomassie dye G-250 (Gel Code Blue Stain, Thermo Scientific). Each lane from the gel was cut and placed in 1.5 mL tubes. Samples were then washed with 250 μL of water, followed by 15 min dehydration in acetonitrile. Proteins were reduced (10mM DTT, 1 hour at 56°C), dehydrated and alkylated (55mM iodoacetamide, 1 hour in the dark). After two rounds of dehydration, trypsin was added to the samples and incubated overnight at 37°C. Peptides were extracted with acetonitrile, dried down and reconstituted in 10% formic acid prior to MS analysis.

Samples were analyzed on an Orbitrap Q-Exactive mass spectrometer (Thermo Fisher Scientific) coupled to an Agilent 1290 Infinity LC (Agilent Technologies). Peptides were loaded onto a trap column (Reprosil pur C18, Dr. Maisch, 100 μm × 2 cm, 3 μm; constructed in-house) with solvent A (0.1% formic acid in water) at a maximum pressure of 800 bar and chromatographically separated over the analytical column (Poroshell 120 EC C18, Agilent Technologies, 100 μm x 50 cm, 2.7 μm) using 90 min linear gradient from 7% to 30% solvent B (0.1% formic acid in acetonitrile) at a flow rate of 150 nL min^{-1}. The mass spectrometers were used in a data-dependent mode, which automatically switched between MS and MS/MS. After a survey scan from 375 to 1600 m/z the 10 most abundant peptides were subjected to HCD fragmentation. MS spectra were acquired with a resolution > 30,000, whereas MS2 with a resolution > 17,500.

Raw data files were converted to mgf files using Proteome Discoverer 1.4 software (Thermo Fisher Scientific). Database search was performed using the *C. elegans* or the human database and Mascot (version 2.5.1, Matrix Science, UK) as the search engine. Carbamidomethylation of cysteines was set as a fixed modification and oxidation of methionine was set as a variable modification. Trypsin was set as cleavage specificity, allowing a maximum of two missed cleavages. Data filtering was performed using a percolator, resulting in 1% false discovery rate (FDR). Additional filters were search engine rank 1 and mascot ion score > 20.

Crapome[68] was used to analyze BBLN-1 interacting proteins in three biological replicas and bublin binding proteins in a single experiment, using proteins identified in the GFP pull downs as control. Significance analysis of interactome (SAINT) score[69] and simpler fold-change (FC) calculations FC-A and FC-B were derived from the Crapome analysis by averaging the spectral counts across the controls. FC-A averages the counts across all controls while the more stringent FC-B takes the average of the top 3 highest spectral counts for the abundance estimate.

Antibodies and Immunofluorescence Cell Staining

We used rabbit polyclonal antibodies against bublin (Sigma-Aldrich Cat# HPA020725, RRID: AB_1845816), mouse monoclonal antibodies against PCNT (Abcam Cat# ab28144, RRID: AB_2160664), and rat monoclonal antibodies against tyrosinated α-tubulin (YL1/2; Thermo Fisher Scientific Cat# MA1-80017, RRID: AB_2210201) and KRT8 (DSHB Cat# TROMA-I, RRID: AB_531826). We used Alexa Fluor 568-conjugated Phalloidin to stain actin (Life Technologies). We used Alexa Fluor 488-, 594- and 647-conjugated goat antibodies against respectively mouse, rabbit and rat (Life Technologies) as secondary antibodies.

HeLa cells were fixed with −20°C methanol or 4% PFA for 10 min and permeabilized with 0.1% Triton X-100 in phosphate-buffered saline (PBS) for 10 min. Subsequent washing and labeling steps were carried out in PBS supplemented with 2% bovine serum albumin and 0.05% Tween-20. Slides were rinsed in 70 and 100% ethanol and mounted in Vectashield mounting medium supplemented with DAPI (Vector Laboratories).

Mouse small intestinal organoids were fixed in suspension using ice-cold 4% PFA (Aurion) and immunolabeled as described previously.[70]

QUANTIFICATION AND STATISTICAL ANALYSIS

Image analysis

Invagination numbers in *bbln-1(null)* animals were counted manually from intestinal rings int2 to int4, using Z stacks that span the entire intestinal lumen. Invagination widths were measured by determining the full width at half-maximum of an intensity plot drawn across the center of the invagination in an orthogonal view. Corresponding cell lengths were quantified by drawing a spline through the lumen from lateral membrane to lateral membrane. Intensity distribution profiles of fluorescent proteins at the apical domains of the intestine or organoids were obtained by performing a 40-pixel (4.7 μm) wide line-scan perpendicular to the apical membrane. GFP::BBLN-1 intensity at the apical domain was determined by taking the maximum intensity value of a 40-pixel wide line-scan perpendicular to the apical membrane, and subtracting the mean background intensity (measured in a 40-pixel diameter circle outside of the worm). Each data point shown represents the average of 6–8 measurements per animal. All images were analyzed and processed using ImageJ alone (spinning disk) or in combination with Zen Black software (Airyscan).

Quantification of brood size and lethality

Starting at the L4 stage, individual P0 animals were cultured at 20°C and transferred to a fresh plate every 24 hours for 6 days. Hatched and unhatched progeny were scored 24 hours after removal of the P0, and larval lethality was scored 48 hours after removal of the P0.

Statistical analysis

All statistical analyses were performed using GraphPad Prism 8. For population comparisons, a D'Agostino & Pearson test of normality was first performed to determine if the data was sampled from a Gaussian distribution. For data drawn from a Gaussian distribution, comparisons between two populations were done using an unpaired t test, with Welch's correction if the SDs of the-populations differ significantly, and comparisons between > 2 populations were done using a one-way ANOVA if the SDs of the populations differ significantly. For data not drawn from a Gaussian distribution, a non-parametric test was used (Mann-Whitney for 2 populations and Kruskal-Wallis for > 2 populations). ANOVA and non-parametric tests were followed up with multiple comparison tests of significance (Dunnett's, Tukey's, Dunnett's T3 or Dunn's). Tests of significance used and sample sizes are indicated in the figure legends. No statistical method was used to pre-determine sample sizes. No samples or animals were excluded from analysis. The experiments were not randomized, and the investigators were not blinded to allocation during experiments and outcome assessment.